Laser-induced magnetostriction in rare-earth metals probed by UXRD

Untersuchung laserinduzierter Magnetostriktion an Seltenen Erden mit Hilfe ultraschneller Röntgenbeugung

Florian Baltrusch

Universitätsmasterarbeit
zur Erlangung des akademischen Grades

Master of Science
(M. Sc.)

im Studiengang
Physik

eingereicht am 11. November 2024 im
Fachgebiet der ultraschnellen Dynamik in kondensierter Materie
am Institut für Physik und Astronomie
der Universität Potsdam

1. Gutachter	Prof. Dr. Matias Bargheer
2. Gutachter	PD Dr. Klaus Habicht
Betreuer	Dr. Steffen Peer Zeuschner

"You can never know everything, and part of what you know is always wrong. Perhaps even the most important part. A portion of wisdom lies in knowing that. A portion of courage lies in going on anyway."

— Robert Jordan

Abstract

This thesis investigates and compares the lattice response of 40 nm rare-earth thin-film heterostructures upon femtosecond optical excitation at temperatures above and below the magnetic ordering temperatures in Gd, Tb and Dy. Ultrafast X-ray diffraction at our laboratory-based plasma X-ray source is employed, which reveals the strain dynamics on a picosecond timescale, as well as thermal expansion and heat conductivity on a nanosecond timescale. In the paramagnetic phase above the magnetic ordering temperature, a conventional metallic expansive response is observed, as the excitation energy is deposited in the electronic and phononic subsystem. Below the magnetic ordering temperature, the coupling between the magnetic subsystem and the lattice leads to a competition between the expansive stress from electrons and phonons and the contractive stress from spin excitations. This results in negative thermal expansion, observed in Gd, Tb, and Dy below their respective magnetic ordering temperatures, which was revealed using X-ray diffraction at the KMC-3 XPP endstation at BESSY II. This magnetostrictive effect can be attributed to the indirect RKKY interaction, which occurs in Gd, Tb and Dy.

To separate the stress contributions of the three subsystems on an ultrafast timescale, the thermal lattice expansion and heat capacities of Gd, Tb, and Dy in equilibrium in terms of an extended Grüneisen model are investigated. The Grüneisen parameters of the phononic and magnetic subsystems in terms of a three-energy-model were determined, which allows the extraction of the time-dependent energy distribution and driving stresses. The results are in agreement with the modelled strain response via a linear-chain-model in the paramagnetic phase with a one-energy-model. However, the magnetic Grüneisen parameters of Gd and Tb turned out to be temperature-dependent, which reveals the limitations of the Grüneisen modelling. This temperature-dependence yields intriguing effects, as for the Tb layer, an ultrafast invar behaviour of the strain response has been observed under certain excitation conditions. The delayed laser-induced contraction of Gd indicates a demagnetisation on a timescale of 50 ps, which is slower compared to Tb and Dy, which have a demagnetisation timescale of approximately 8 ps and 20 ps respectively. These findings align closely with recent femtosecond X-ray magnetic circular dichroism (XMCD) results.

Kurzdarstellung

In dieser Arbeit wird das Verhalten von 40 nm dünnen Schichten Seltener Erden nach einer optischen Anregung mit Femtosekunden-Laserpulsen oberhalb und unterhalb der magnetischen Ordnungstemperaturen in Gd, Tb und Dy betrachtet. Mit Hilfe ultraschneller Röntgenbeugung an einer Laser-getriebenen Plasmaröntgenquelle lassen sich die Ausdehnungsdynamiken im Pikosekundenbereich, sowie die thermische Ausdehnung und Wärmeleitfähigkeit im Nanosekundenbereich untersuchen. In der paramagnetischen Phase oberhalb der magnetischen Ordnungstemperatur wird eine konventionelle metallische Expansion beobachtet, da die Anregungsenergie dem elektronischen und phononischen Teilsystem zugeführt wird. Die Kopplung des magnetischen Teilsystems mit dem Gitter führt unterhalb der magnetischen Ordnungstemperatur zu einem Entgegenwirken der durch Elektronen und Phononen getriebenen Gitterausdehnung. Daraus resultiert eine negative thermische Ausdehnung, die in Gd, Tb und Dy unterhalb ihrer magnetischen Ordnungstemperatur mittels Röntgenbeugung am BESSY II nachgewiesen wurde. Dieser magnetostriktive Effekt kann auf die indirekte RKKY-Wechselwirkung zurückgeführt werden, die in Gd, Tb und Dy auftritt.

Um die Druckbeiträge der drei Teilsysteme auf einer ultraschnellen Zeitskala zu separieren, werden die thermische Ausdehnung und die Wärmekapazitäten von Gd, Tb und Dy im Gleichgewicht im Rahmen eines erweiterten Grüneisenmodells untersucht. Die Grüneisenparameter der phononischen und magnetischen Teilsysteme wurden im Rahmen eines Drei-Energie-Modells bestimmt, mit dem die zeitabhängige Energieverteilung und die treibenden Drücke separiert werden können. Die Ergebnisse stimmen mit der simulierten Ausdehnung in der paramagnetischen Phase unter Verwendung eines Ein-Energie-Modells überein. Allerdings erwiesen sich die magnetischen Grüneisenparameter von Gd und Tb als temperaturabhängig, was die Grenzen der Grüneisenmodellierung aufzeigt. Diese Temperaturabhängigkeit führt zu verblüffenden Effekten, da für die Tb-Schicht unter bestimmten Anregungsbedingungen ein ultraschnelles Invar-Verhalten der Ausdehnung beobachtet wurde. Die verzögerte laserinduzierte Kontraktion von Gd deutet auf eine Demagnetisierung auf einer Zeitskala von 50 ps hin, was im Vergleich zu Tb und Dy, die Demagnetisierungszeitskalen von ungefähr 8 ps bzw. 20 ps aufweisen, langsamer ist. Dies steht im Einklang mit durch XMCD gewonnenen zeitgenössischen Ergebnissen.

Acknowledgments

As my Master's project comes to an end, I would like to express my gratitude to the people who supported and guided me throughout this journey.

First, I would like to thank Prof. Dr. Matias Bargheer, the head of our research group, for creating a pleasant and encouraging working environment. His thoughtful advice and productive discussions were invaluable in improving my work, and I appreciate the time and care he dedicates to address concerns promptly and effectively.

I am extremely grateful to my supervisor, Dr. Steffen Peer Zeuschner, for his patience and constant support. His expertise in experimental setups, combined with his thorough and constructive feedback, greatly aided me during both the research and writing phases of my work.

Special thanks are due to Dr. Alexander von Reppert, whose invaluable advice on software like Python significantly enhanced my work. His keen eye for detail and precision in scientific writing has been a source of inspiration, and I am grateful for the time and energy he devoted to helping me, despite not being my official supervisor.

I am also thankful to Dr. Maximilian Mattern, who guided me through the early stages of my thesis, introducing me to Python and helping me quickly grasp the topic. His sharp and competent explanations and work ethic were truly inspiring.

Dr. Marc Herzog, although not directly involved in my thesis, played a key role as IT administrator, ensuring my smooth integration into the group. I am excited about my upcoming PhD project under his supervision.

Thanks to Dr. Matthias Rössle and Dr. Florin Boariu for ensuring the success of my project at BESSY II and for their valuable insights into programming.

Finally, I would like to thank the entire research group for providing such a positive, competent, and highly supportive working atmosphere.

Above all, I am deeply grateful to my family for their unconditional support in everything I do. Without them, none of this would have been possible.

Abbreviations

Table 1: This table contains all abbreviations used in this thesis in alphabetical order.

Abbreviation	Meaning
AFM	helical antiferromagnetic
Al_2O_3	sapphire
Dy	dysprosium
FM	ferromagnetic
fs	femtosecond
Gd	gadolinium
Ho	holmium
LASER	light amplification by stimulated emission of radiation
LTE	linear thermal expansion
Lu	lutetium
Nb	niobium
NTE	negative thermal expansion
PM	paramagnetic
ps	picoseconds
PXS	plasma X-ray source
RKKY	Ruderman-Kittel-Kasuya-Yosida
RSM	reciprocal space map
RSS	reciprocal space slice
Tb	terbium
Ti:Sa	titanium-sapphire
UXRD	ultrafast X-ray diffraction
XMCD	X-ray magnetic circular dichroism
XRD	X-ray diffraction
Y	yttrium

Contents

1 Introduction

The concept of the atom, as the smallest indivisible unit of matter, traces back to the ancient Greeks. Philosophers such as Democritus theorised that everything in the universe was composed of these fundamental building blocks. Although these ideas lacked the empirical evidence to prove their existence, they laid the foundation for centuries of scientific investigation. Over 2400 years later, our understanding of atomic particles has led to groundbreaking technological advancements. The study of the properties of various elements gained crucial insights into electronic behaviour, lattice vibrations, and magnetism, which drive modern technology. One of them was the discovery of the giant magnetoresistance effect by Peter Grünberg and Albert Fert, for which they were awarded the Nobel Prize in Physics in 2007. Their pioneering work in this field revolutionised data storage technology, which lays the foundation for highly efficient read-write heads in hard disk drives. The application of the giant magnetoresistance effect enabled the development of gigabyte-scale hard drives, which are now an essential part of modern life (Gross & Marx [1]). Another recent breakthrough in data storage is the technique of heat assisted magnetic recording (HAMR), which uses lasers to briefly heat the magnetic data storage medium. This allows for data storage with higher density without the sacrifice of stability or speed. Data storage technologies often face a trilemma: balancing stability, speed, and high data density. The enhancement of one aspect may come at the cost of another. For example, increasing data density can lead to reduced stability, while improving speed may affect the long term data preservation (Wood [2]).

Our research group has conducted numerous experiments on ultrafast magnetostriction, primarily in dysprosium (Dy) and holmium (Ho) ([3–6]), while other research groups have explored magnetostriction in different materials ([7–10]). These observed ultrafast processes are particularly relevant for the increasingly fast-paced demands of data processing. The goal of this thesis is to analyse the rare-earth metals gadolinium (Gd) and terbium (Tb) and compare their ultrafast magnetostriction to Dy. Different demagnetisation time-scales of those materials have already been observed ([11–13]).

My thesis is divided into two parts. Part I covers the fundamentals of magnetostriction in chapter 2, such as the RKKY interaction and the three-energy-model, and the

underlying theory to understand ultrafast X-ray diffraction (UXRD) in chapter 3. UXRD is the utilised technique to resolve the motion of atoms in a crystalline arrangement, which our research group has optimised (Zamponi *et al.* [14] and Schick *et al.* [15]). Part II of my thesis focuses on the experimental results. The temperature-resolved experiments of the Gd, Tb and Dy thin-films, carried out at the KMC-3 XPP endstation at BESSY II, are presented in chapter 4, with the result of extracted Grüneisen parameters for Gd, Tb and Dy. Time-resolved experiments at the same materials were conducted at our laboratory based plasma X-ray source, which is introduced in chapter 5. I showed that Gd, Tb and Dy all exhibit negative thermal expansion below their magnetic ordering temperature.

Part I

Fundamentals

2 Models of magnetostriction

Spontaneous magnetostriction is the expansion or contraction of the crystal lattice as a function of the magnetisation. This chapter will introduce the rare-earth materials, which are subject to test in this thesis, as well as the concepts of magnetostriction. The underlying models, such as the three-energy-model, which apply to these systems will also be covered.

2.1 Magnetostriction in rare-earth metals

Rare-earth metals are known to exhibit giant magnetostriction ([3–6]). The three samples analysed in this thesis are depicted in figure 2.1. Those three heterostructures are related, as they are structurally the same. Only the 40 nm thin-film rare-earth layer differs in the rare-earth element: gadolinium (Gd), terbium (Tb), or dysprosium (Dy). The samples are therefore labelled accordingly as Gd sample, Tb sample, and Dy sample. Each sample has a 10 nm yttrium (Y) capping layer on top, followed by the respective rare-earth layer. Below that, a 50 nm niobium (Nb) layer is present, which is located on top of a 1 mm thick sapphire (Al_2O_3) substrate. The Yttrium layer on top prevents oxidation of the rare-earth layer, while the Nb layer functions as a buffer layer during the growth and as a detection layer for ultrafast strain, as described in Mattern *et al.* [5].
The magnetostriction of the rare-earth layer can be measured as a function of the temperature and as a function of the time-delay between the pump and the probe pulse, which is described in section 5.1. During the quasi-static measurements, the change of the distance between the rare-earth atoms along the *c*-axis is recorded temperature-dependently. The top of each sample is the Y layer, which corresponds to the direction from which the samples are excited by a laser pulse when time-resolved measurements in terms of a pump-probe experiment are conducted (section 5.1). Two exemplary experimental results of magnetostriction are illustrated in figure 2.2. Figure 2.2 (a) depicts the temperature-resolved distance of the lattice planes, which corresponds to the *c*-axis of the hexagonal crystal structure. The usually expected behaviour of linear thermal expansion (LTE) is interrupted between roughly 150 K and 250 K, which is due to magnetostriction. Figure 2.2 (b) shows the time-resolved development of the *c*-axis after laser excitation. For a

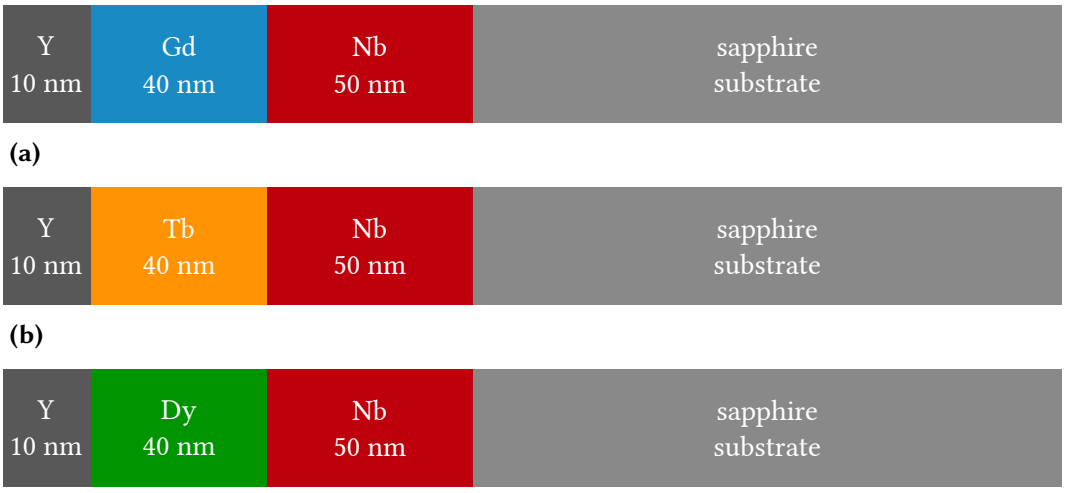

Figure 2.1: These samples were manufactured by Karine Dumesnil, Institut Jean Lamour, Université Lorraine, Nancy. (a) shows the structure of the Gd sample, (b) depicts the structure of the Tb sample, and (c) illustrates the structure of the Dy sample.

selected starting temperature in the ferromagnetic (FM) phase, laser-induced spontaneous magnetostriction can be observed as an ultrafast contraction along the *c*-axis. This is not the case if the starting temperature lies in the paramagnetic (PM) phase.

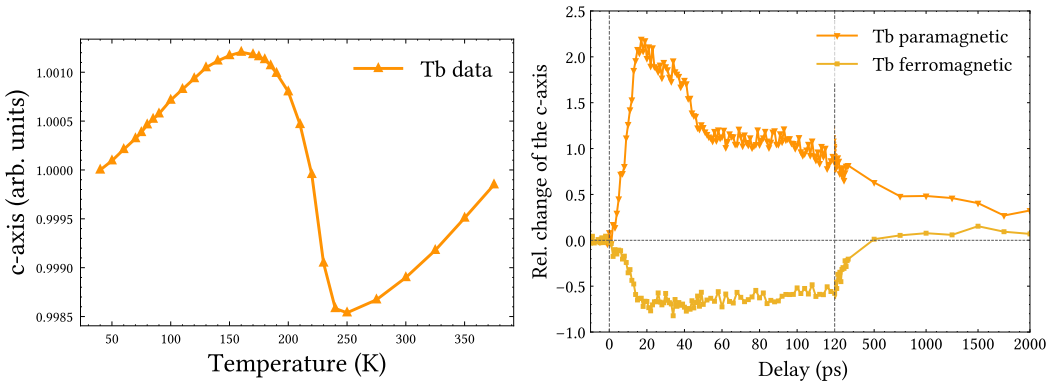

Figure 2.2: (a) The interrupted thermal expansion of the *c*-axis between 150 K and 250 K is depicted temperature-resolved. (b) The time-resolved change of the *c*-axis depends on whether Tb is paramagnetic or ferromagnetic.

In general, a distinction is made between different types of magnetostriction. If magnetostriction occurs due to a change in temperature, e.g. upon laser excitation, this is named *spontaneous magnetostriction* or just magnetostriction. This is the type of magnetostriction mainly discussed in this thesis. When an external magnetic field is applied to a sample, that can lead to *forced magnetostriction*, which is another form of magnetostriction. This will be mentioned briefly in chapter 6. The main mechanism of magnetostriction in rare earths is *exchange striction* mediated by an indirect RKKY interaction, as presented in section 2.1. Another mechanism of magnetostriction is *anisotropy striction*, presented in section 2.1, which is *not* the main mechanism in rare-earth metals but can possibly still explain why various rare earths exhibit different magnetostrictive behaviours.

RKKY exchange interaction

As the magnetic moments of the rare earths are carried by the 4f-electrons whose orbitals have practically no overlap, an indirect mechanism of exchange is necessary, which then mediates the exchange striction. This indirect interaction is entitled as RKKY interaction, named after Malvin Avram Ruderman, Charles Kittel, Tadao Kasuya and Kei Yosida. The coupling is realised via conduction band electrons, as the magnetic moments orient the spin of the conduction band electrons, which in turn orient the magnetic moments of the neighbouring ions (Hunklinger [16]). According to Skomski [17], the RKKY interaction is proportional to

$$J(r) \sim \frac{\sin(2k_F r) - 2k_F r \cos(2k_F r)}{(2k_F r)^4}, \tag{2.1}$$

where k_F is the Fermi vector, r is the distance between neighbouring ions and J is the exchange coefficient. In the Heisenberg model, according to Gross & Marx [1], the spin-dependent Hamiltonian $\mathcal{H}$ can be expressed as:

$$\mathcal{H} = -\sum_{j \neq i, i > j} J_{ij} \frac{1}{\hbar^2} \vec{S}_i \cdot \vec{S}_j. \tag{2.2}$$

The distance-dependent exchange coefficient $J(r)$ is illustrated in figure 2.3. This implies that the state of the spin system is directly connected to the distance of the ions, which can lead to magnetostrictive effects. If $J(r) > 0$, then the vectors $\vec{S}_i$ and $\vec{S}_j$ of the neighbouring spins i, j are aligned parallel, which leads to a ferromagnetic material. If $J < 0$, the vectors are aligned antiparallel, which leads to an antiferromagnetic material. In some cases, the material becomes a helical antiferromagnet, which will in the following be referred to as AFM. This is the

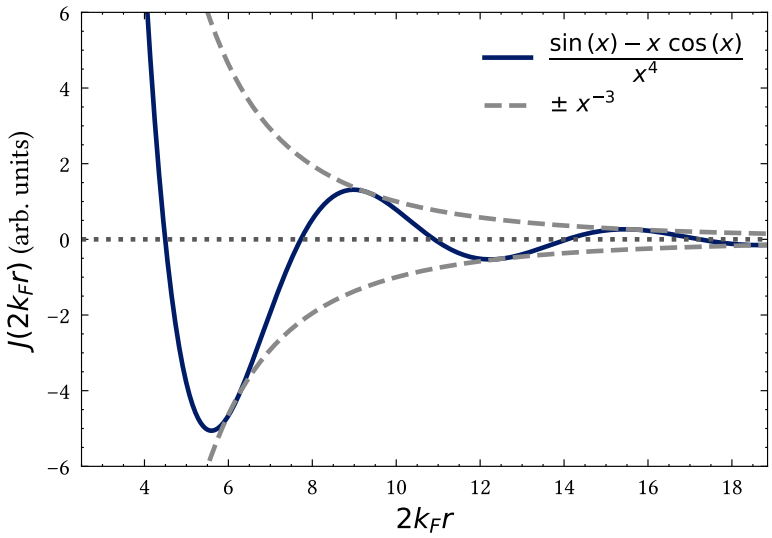

Figure 2.3: The amplitude of the RKKY interaction is distance-dependent. $\pm x^{-3}$ depicts the enveloping function with $x = 2k_F r$.

case for Dy, as illustrated in figure 2.4. The relation between the conventional antiferromagnetic structure and the helical antiferromagnetic structure becomes evident in the two-dimensional projection of the spin spiral, which is also shown in figure 2.4.

Anisotropy striction

According to Engdahl [19], 4f-electrons have a strong spin-orbit coupling, which means that the spin of a 4f-electron is firmly attached to the corresponding electronic cloud. This spin moment is illustrated as $\vec{m}$ in figure 2.5. In a crystal lattice at rest, the magnetic moment points into a certain direction, defined by the neighbouring positively charged nuclei. This tendency of the magnetic moment to point into a preferred direction, because the Coulomb forces from neighbouring ions act on the non-spherical orbital hosting the spin, is called *magnetocrystalline anisotropy*. If the distance between these nuclei changes, consequently the electron orbital may change and thus tilt the direction the magnetic moment points to. This is also true in reverse, as the application of an external magnetic field can rotate the magnetic moment and consequently the electron orbit, which would therefore change the distance between the nuclei.

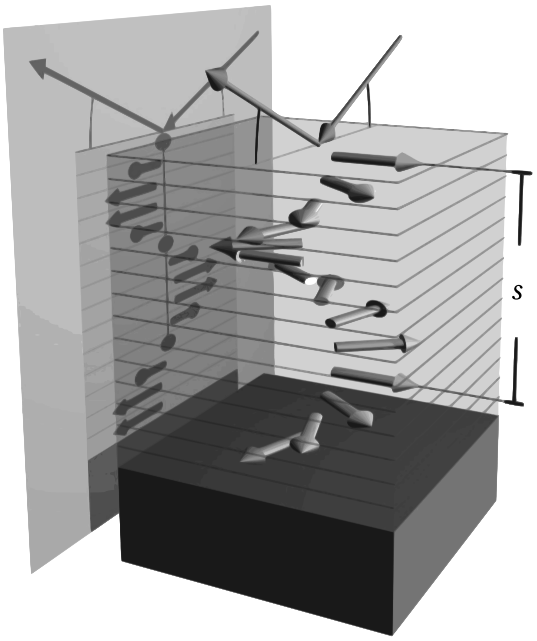

Figure 2.4: Between the Curie and the Néel temperature, the structure of Dy is helical antiferromagnetic. The periodicity of the spin spiral with the length s does not necessarily need to resemble the periodicity of the lattice. Source: Ott [18]

This invoked change of the distance of the lattice planes is called anisotropy striction. The model of anisotropy striction only predicts an impact on the lattice, if the electron orbital that carries the magnetic moment is non-spherical. In Gd, the 4f-orbital is exactly half filled as shown in table 2.1, which leads to a spherical orbital form (Gross & Marx [1]). This illustrates nicely why anisotropy striction is likely *not* the main reason for magnetostriction in rare-earth materials, because the other rare earths exhibit spontaneous magnetostriction with a similar strength as observed in Gd. In these materials, the magnetic moments are carried by 4f-electrons, whose wave function overlap is small due to their proximity to the nucleus (Hunklinger [16]). This is true for the elements Gd, Tb and Dy, as they are neighbours in the periodic table of elements. Their electronic configurations are therefore similar, as depicted in table 2.1.

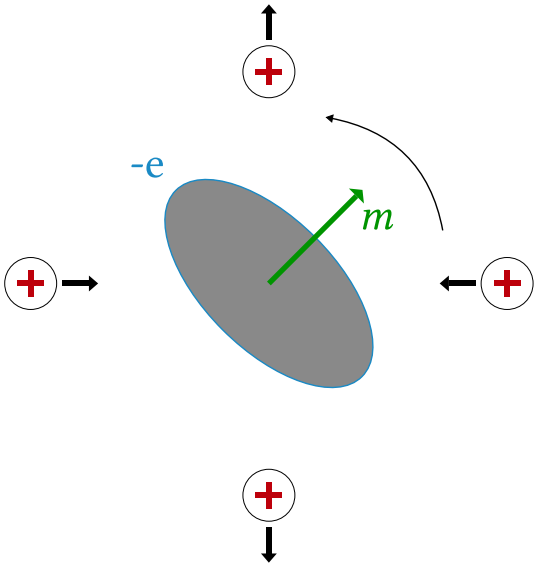

Figure 2.5: The electronic orbital rotates due to an external magnetic field, which changes the position of the positive nuclei. Source: Engdahl [19]

Table 2.1: This table contains the electronic configuration of Gd, Tb and Dy according to Ott [18] and the angular momenta S_{4f}, L_{4f} and J_{4f} of corresponding the 4f-orbital. In Gross & Marx [1], this $(5d6s)^3$ hybridisation is not used.

element	configuration	S_{4f}	L_{4f}	J_{4f}
Gd	$[Xe]4f^7(5d6s)^3$	7/2	0	7/2
Tb	$[Xe]4f^8(5d6s)^3$	3	3	6
Dy	$[Xe]4f^9(5d6s)^3$	5/2	5	15/2

2.2 Lattice dynamics

This section 2.2 will introduce the three-energy-model (3EM) in section 2.2.1, which leads to an extended Grüneisen model and will be applied to the linear-chain-model

in section 2.2.2. The Grüneisen modelling of the quasi-static strain data will be carried out in chapter 4, while the linear-chain-model is used to perform transient simulations of the time-resolved strain measurements, which are discussed in chapter 5.

2.2.1 Three-energy-model

The three-energy-model assumes the lattice of a solid to be impacted by the electronic, phononic and magnetic subsystem, illustrated in blue, orange and green in figure 2.6 respectively.

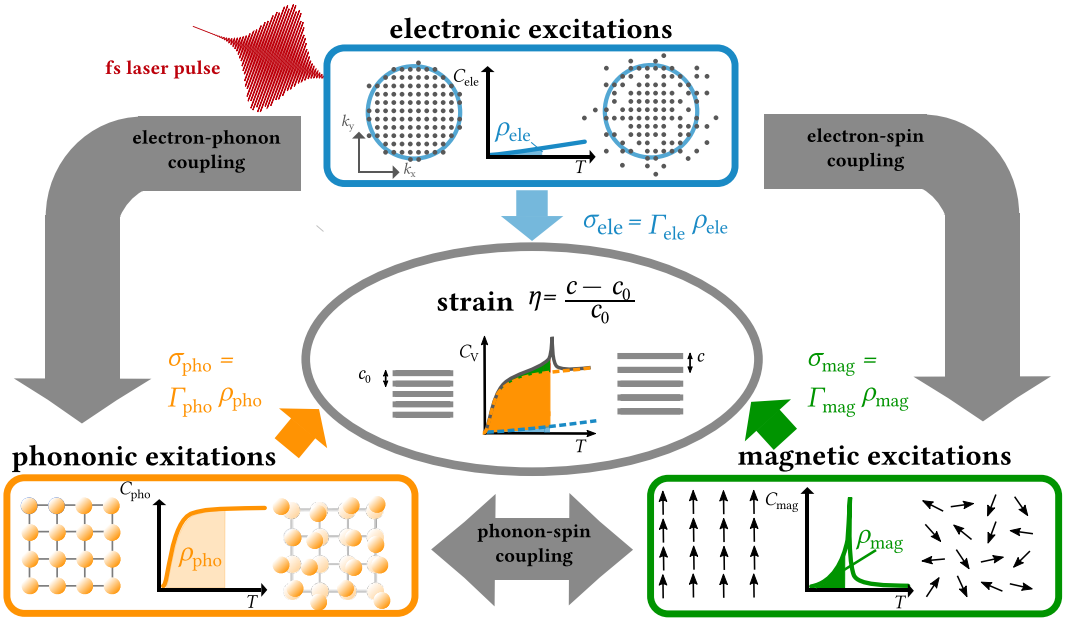

Figure 2.6: The three-energy-model describes the impact of the electronic, phononic and magnetic subsystem on the lattice. The subsystems interact with each other and have their own heat capacity C. Source: Mattern *et al.* [5]

Initially after excitation indicated by the red laser pulse, the electronic subsystem is heated, as the electrons interact with the oscillating electromagnetic field of the laser pulse. An excitation of electrons raises their energy over the Fermi energy, which is illustrated in the pictogram in the blue box. The electronic system can now transfer its energy to the phononic subsystem and to the magnetic subsystem via the corresponding electron-phonon or electron-spin coupling. The efficiency

of this transfer depends on the coupling constants, which are depicted as grey arrows in figure 2.6. The phononic subsystem and the magnetic subsystem can also interact, with an efficiency given by the phonon-spin coupling. An excitation of the phononic system induces lattice vibrations, as illustrated in the pictogram in the orange box. The green box shows the excitation of the magnetic system by disordering the magnetic moments. A distinct temperature T is assigned to each of the three systems immediately after excitation, which will equilibrate over time. Every subsystem has a different energy reservoir, which exerts a pressure on the lattice quantified by the *stress* σ. The stress has the dimensions of an energy density, which is equivalent to a pressure. The stress is given by:

$$\sigma_i = \Gamma_i \rho_i. \tag{2.3}$$

The dimensionless proportionality constant between the stress σ and the energy density ρ is the *Grüneisen parameter* Γ. Each of the three subsystems can influence the interatomic distance c between the layers of the lattice of the solid. The relative change of the layer distance

$$\eta = \frac{c - c_0}{c_0} \tag{2.4}$$

is entitled as the *strain* η. The stress and the strain are related via Hooke's law:

$$\sigma = c\eta. \tag{2.5}$$

When referring to strain, it specifically denotes the out-of-plane strain in this thesis, which is why the elastic constant c is often represented as c_{33}. The separation of the stress contribution of every subsystem on the lattice is captured in an *extended Grüneisen model*. Thus, an individual Grüneisen parameter is assigned to each subsystem.

In a three-temperature-model, each subsystem is assigned a distinct temperature, which indicates that they have not yet reached equilibrium and thus not share a common temperature. However, even when the temperatures are equal, the subsystems still possess three distinct energies, as each subsystem has a different energy density at the same temperature. Since energy density is proportional to stress, I will refer to this model as a three-energy-model, rather than a three-temperature-model, throughout this thesis. The energy densities are related to the heat capacities via equation (2.6).

$$\rho_{\mathrm{E}}(T) = \int_0^T C(T')\, dT'. \tag{2.6}$$

If the heat capacity is given at a constant Volume V, it is called C_V, while when given at constant pressure p it is called C_p. For a non-zero linear thermal expansion coefficient α, the heat capacity at constant volume is always smaller than at constant pressure because no volume work is done through expansion. The following relation, taken from Gross & Marx [1], applies:

$$C_p - C_V = TVB\alpha^2. \tag{2.7}$$

Here, T is the temperature, V the volume and B the bulk modulus, which can be found in table 4.1. At room temperature, $C_p - C_V$ has a magnitude of 10^{-1} for solids.

Electronic heat capacity

In the Sommerfeld model (Hunklinger [16]), the electronic heat capacity is given by:

$$C_V^{ele} \approx \gamma T. \tag{2.8}$$

The values for the Sommerfeld coefficient γ can be found in table 4.1. They are given by the density of electronic states at the Fermi level. It should not be confused with the fine-structure constant $\alpha \approx 1/137$, which is sometimes also called Sommerfeld constant. The linear increase of the electronic heat capacity with the temperature is plotted in figure 2.7 (a). The corresponding energy density is depicted in figure 2.7 (b), which is the integral of the heat capacity according to equation (2.6) .

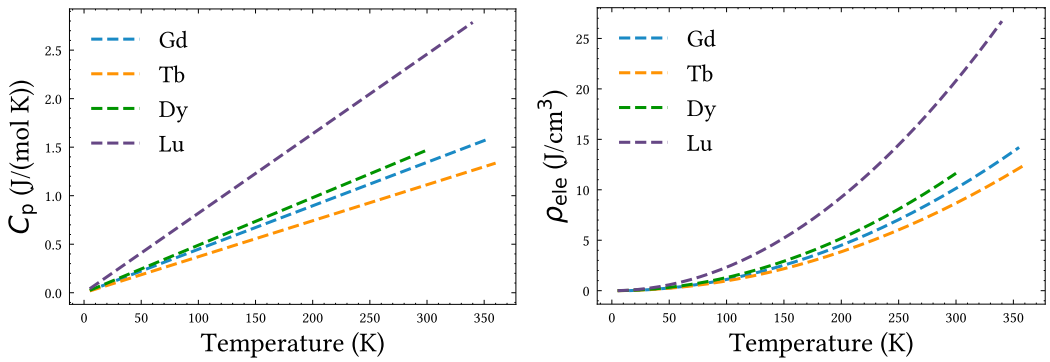

(a) **(b)**

Figure 2.7: (a) The electronic heat capacity increases linearly in temperature. (b) The electronic energy density increases quadratic in temperature.

For the considered materials at 300 K, the energy density of the electronic system

ranges from 10 J/cm^3 to 25 J/cm^3, which small compared to the phononic and magnetic energy densities.

Phononic heat capacity

According to Gross & Marx [1], the phononic heat capacity is given by:

$$C_{\mathrm{V}}^{\mathrm{pho}} = 9R\left(\frac{T}{\Theta_D}\right)^3 \int_0^{\Theta_D/T} \frac{x^4 e^x}{(e^x-1)^2}\, dx = \begin{cases} \sim T^3 & \text{, if } T \ll \Theta_D \\ 3R & \text{, if } T \gg \Theta_D \end{cases}. \tag{2.9}$$

Here, $R = N_A k_B$ is the universal gas constant and Θ_D is the Debye temperature. The proportionality of $C_{\mathrm{V}}^{\mathrm{pho}}$ at low temperatures is called the Debye T^3 law. The thermal energy $k_B T$ at low temperatures can only excite vibrational quanta $\hbar\omega$ within the linear acoustic phonon dispersion. The convergence of $C_{\mathrm{V}}^{\mathrm{pho}}$ at high temperatures is the Dulong–Petit law. The limit of $3R$ originates from the three possible vibration directions in three dimensions, which accounts for both potential and kinetic energy contributions. Both the Debye T^3 law and the Dulong–Petit law can be identified in figure 2.8 (a). The calculated heat capacities look very similar for Gd, Tb, Dy and Lu, but a comparison of the corresponding energy densities in figure 2.8 (b) reveals slight differences.

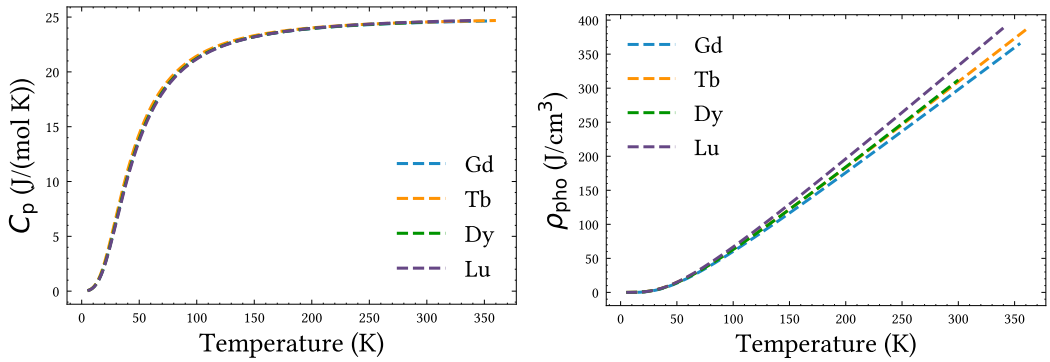

(a) **(b)**

Figure 2.8: (a) The phononic heat capacities are proportional to T^3 at low temperatures and convergence against the limit of $3R$ at high temperatures. (b) Clearer distinctions between the phononic heat capacities of the rare-earth materials become apparent, when the phononic energy densities are compared.

At 300 K, the phononic energy densities for the considered materials range from 300 J/cm^3 to 400 J/cm^3. Well beyond the coupling time of the electronic and phononic

subsystems, the phononic energy density is much larger than the electronic energy density, which validates the idea of a two-energy-model.

Magnetic heat capacity

The magnetic heat capacity can be extracted from the total heat capacity. This is done in section 4.3. The results are depicted in figure 2.9.

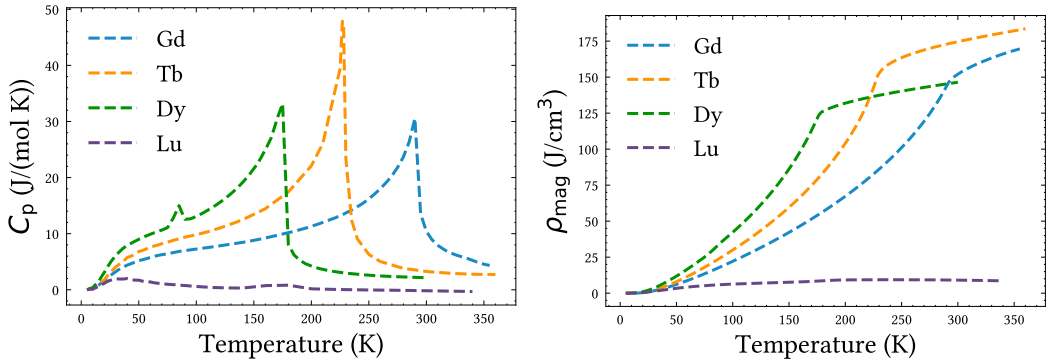

(a) **(b)**

Figure 2.9: (a) The magnetic heat capacities at constant pressure show a maximum at the phase transition temperatures. (b) The plot of the magnetic energy density reveals that even above the magnetic ordering temperature, small amounts of energy can still be deposited into the magnetic system.

The heat capacity of the magnetic system can be approximated by the mean-field theory. Here, the magnetisation M of a ferromagnet is given by the self-consistent equation (2.10):

$$M(T) = \tanh\left(\frac{MT_C}{T}\right). \tag{2.10}$$

The phase transition temperature T_C marks the point where a ferromagnet transitions to the paramagnetic state. In the case of a ferromagnet, this is known as the Curie temperature and for antiferromagnets this temperature is called the Néel temperature. Then M must be interpreted as the sublattice magnetisation. According to Mattern *et al.* [20], the following relation applies to the magnetic heat capacity:

$$C_V \sim M \frac{\partial M}{\partial T}. \tag{2.11}$$

The magnetisation and the magnetisation multiplied by its derivative in respect to the temperature is depicted in figure 2.10. Hence, the result of the mean field model in figure 2.10 only provides a qualitative assessment of the magnetic heat capacity. Therefore, for further analysis, experimental data were taken as shown in figure 4.3.

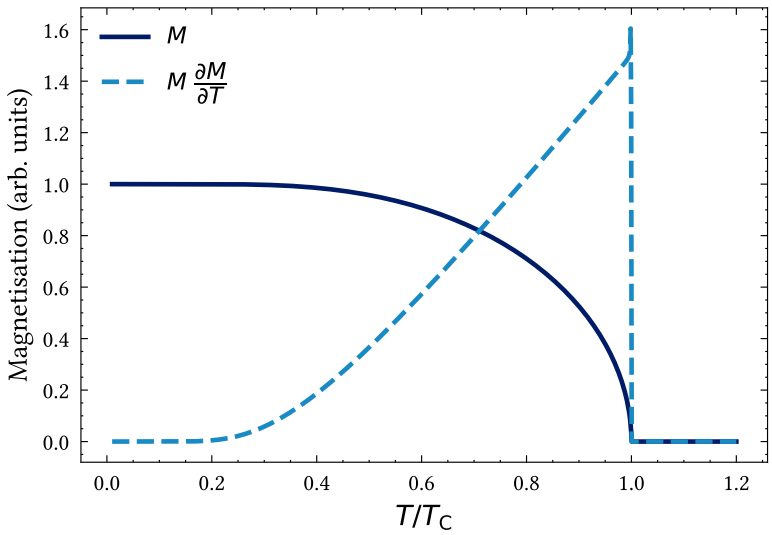

Figure 2.10: The qualitative magnetisation of a ferromagnet is described by the dark blue line. The dashed light blue line indicates the qualitative behaviour of the magnetic heat capacity.

2.2.2 Linear-chain-model

The linear-chain-model represents a solid as a one-dimensional chain of masses and springs. A displacement of such a mass from the equilibrium position leads to an oscillation of the chain. The resulting set of differential equations can be solved numerically. When the solid is heated upon laser excitation, energy is imparted to the system. In the paramagnetic state, this leads to an instantaneous compression of the springs, as the added energy is modelled by inserted spacer sticks into the linear chain, whose atoms cannot move instantaneously. The relaxation of the springs causes an expansion of the linear chain as illustrated in figure 2.11 (a). The amount of energy deposited in each chain, i.e. the length of the spacer sticks, is given by an absorption profile, depicted in figure 2.11 (b). As the intensity of the incident light decays exponentially according to the Lambert-Beer law, the springs

at the surface of the sample usually show the most pronounced contraction, i.e. the longest spacer sticks are inserted. Therefore, the pressure which acts from above on a mass in the linear-chain-model is larger than the pressure which acts from below. This difference induces a compression wave that traverses through the material. The reflection of this wave at the surface of the sample creates a bipolar strain wave, where the expansive part is preceded by a contractive part (Mattern *et al.* [5]). The LTE originates from the contributed energy density of the excitation laser pulse, as implied by equation (2.3).

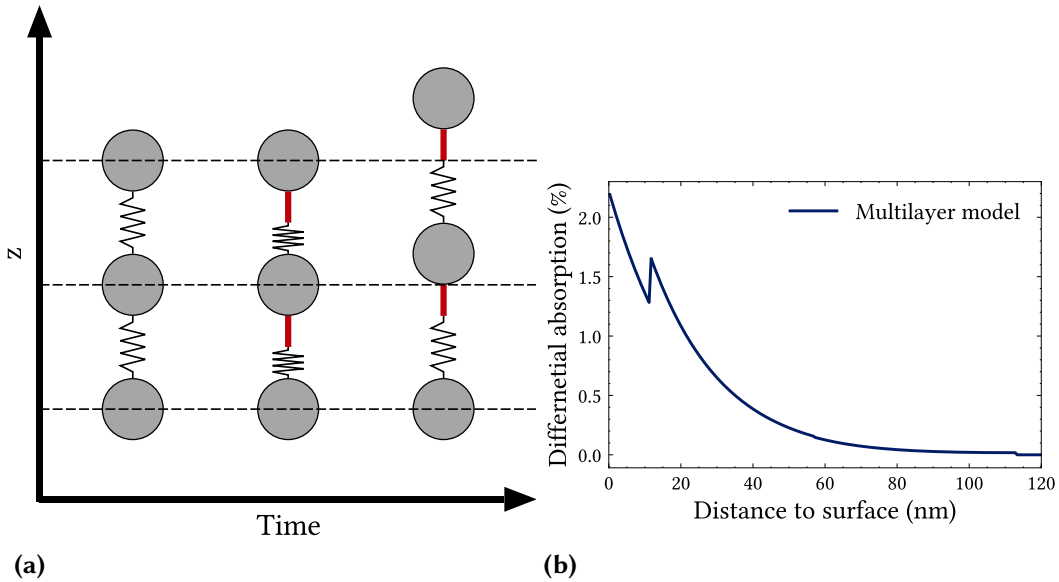

Figure 2.11: (a) The linear-chain-model with one-dimensional masses and springs is illustrated. The length of the red spacer sticks in the linear-chain-model depends on the amount of energy deposited into the system, given by the absorption profile. (b) A multilayer laser absorption profile of the Tb sample is depicted. The discontinuities in the absorption profile originate from interfaces between different materials of the sample.

When thin-films are excited on ultrafast timescales, it has to be taken into consideration that the laterally homogeneous excitation of the laser pulse prevents an expansion of the thin-film in the in-plane directions. This leads to an enhanced expansion out-of-plane, described by a change of the Grüneisen parameter for purely out-of-plane dynamics. This enhanced expansion is known as the *Poisson effect*. A Poisson correction is therefore to be made, which can be quantified according to von Reppert *et al.* [4]:

$$\text{Poisson correction factor for } \Gamma_{\text{pho}} : 1 + \frac{c_{13}}{c_{33}} \frac{2\alpha_{\parallel}}{\alpha_{\perp}}. \tag{2.12}$$

$$\text{Poisson correction factor for } \Gamma_{\text{mag}} : 1 - \frac{c_{13}^2}{(c_{11} + c_{12})c_{33}}. \tag{2.13}$$

The values to insert here are found in table 5.3. For the positive phononic Grüneisen parameter Γ_{pho}, the prevented in-plain expansion leads to a stronger out-of-plane expansion. As will be discussed in section 4.5.4, the magnetic Grüneisen parameter Γ_{mag} in Gd, Tb and Dy is negative. Accordingly, the absolute value of the magnetic Grüneisen parameter is decreased when the Poisson correction is applied, because the out-of-plane contraction would require an expansion in-plane, which is hindered.

3 Scattering theory

This chapter will cover the fundamentals of scattering theory involved in ultrafast X-ray diffraction (UXRD). This includes the basics of crystallography and structural analysis. Of special importance is the concept of reciprocal space and the von Laue condition, which is an observation condition for diffraction peaks to determine the interatomic distance, i.e. the lattice constants. This chapter also covers the data acquisition routine to evaluate the quasi-static and transient changes in the lattice constant of materials. The sections 3.1 and 3.2 are adapted from Gross & Marx [1] and Hunklinger [16].

3.1 Crystal structure

The periodically recurring structure of a crystal is called the *basis*. The number of atoms in the basis depends on the examined material. The basis of most metals is composed of one atom, while the basis of complex Protein crystals contains up to 10^4 atoms (Hunklinger [16]). Even if only one type of atom is present in a material, the basis can still be diatomic, as in graphene. Every basis can be reduced to one point in space. Those *lattice points* form a point lattice, but those points do *not* necessarily have to be the locations of the atoms of the crystal.

An arbitrary point at the location $\vec{r}$ inside the crystal has the environment $\mathcal{E}$. The *lattice vector* $\vec{R}$ is defined in such a way that it points to an equivalent environment in space, which means:

$$\mathcal{E}(\vec{r}) = \mathcal{E}(\vec{r} + \vec{R}). \tag{3.1}$$

$\vec{R}$ is defined as

$$\vec{R} = n_1\vec{a}_1 + n_2\vec{a}_2 + n_3\vec{a}_3 \qquad n_i \in \mathbb{Z}. \tag{3.2}$$

The vectors $\vec{a}_i$ are the *basis vectors* of the point lattice and hence represent its symmetry. They therefore do *not* define the actual position of the basis atoms. The lengths of the basis vectors are often called *lattice constants*. The basis vectors form a parallelepiped, which is called the *unit cell*. The volume of this unit cell is $V_c = (\vec{a}_1 \times \vec{a}_2) \cdot \vec{a}_3$. Stringing together a sequence of unit cells forms the complete

crystal without overlaps. *Primitive unit cells* are the smallest possible unit cells that contain only one lattice point, which often lies in its origin. Unlike a *conventional unit cell*, which contains more than one lattice point, the primitive unit cell often does not fully capture the symmetry of the lattice. An example for that is shown in figure 3.1 (a).

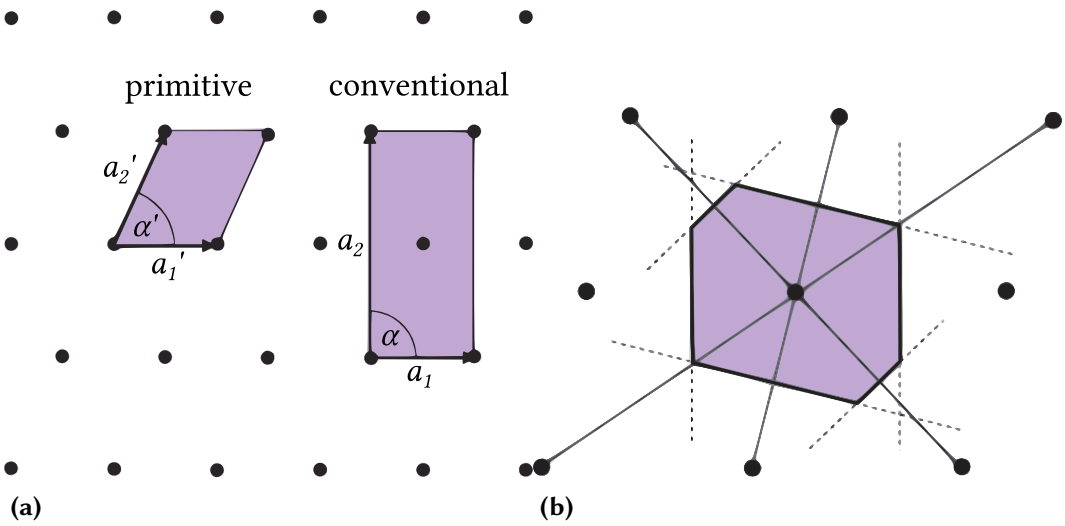

Figure 3.1: (a) The primitive unit cell has its lattice point in its origin. The conventional unit cell contains more than one lattice point. (b) The Wigner-Seitz cell has its lattice point in its centre. Source: Hunklinger [16].

The rectangular conventional unit cell in figure 3.1 (a) contains two lattice points and is therefore not primitive. The primitive unit cell does not represent the symmetry of the point lattice. The unit cells with the highest symmetry in three dimensions form the 14 *Bravais lattices*. A Bravais lattice is an infinitely extended lattice that looks the same from every grid point. In some cases, it is advantageous when the unit cell has its lattice point in its centre and not like the parallelepiped in its origin. That is why the most frequently used primitive unit cell is the *Wigner-Seitz cell*. The Wigner-Seitz cell covers the area around a lattice point that is closer to this lattice point than all other lattice points. When one constructs the Wigner-Seitz cell, all geometric medians of the imaginary lines between the lattice points have to be connected. This is depicted in figure 3.1 (b).

3.2 Structural analysis

Each sample has an *electron density distribution* $\varrho(\vec{r})$. Similar to equation (3.1), the periodicity conditions of the crystal also apply to the electron density distribution:

$$\varrho(\vec{r}) = \varrho(\vec{r} + \vec{R}). \tag{3.3}$$

In the case of X-ray diffraction (XRD), the electrons of the atoms act as the scattering centres. If a plane wave hits such a scattering centre, it becomes the origin of a spherical wave. The connection between the *scattering amplitude* $\mathcal{A}(\vec{Q})$ and the electron density distribution $\varrho(\vec{r})$ is:

$$\mathcal{A}(\vec{Q}) = \int_{V_s} \varrho(\vec{r})\, e^{-i\vec{Q}\cdot\vec{r}}\, dV. \tag{3.4}$$

Here, $\vec{Q} = (q_x, q_y, q_z)$ is the *scattering vector* with $\vec{Q} = \vec{k}' - \vec{k}$ and V_s is the volume of the sample. The scattering vector is visualised in figure 3.2 as the difference of the $\vec{k}$-vectors between the outgoing and incoming photons. According to equation (3.4), $\mathcal{A}(\vec{Q})$ is the Fourier transform of $\varrho(\vec{r})$. In principle, one could transform back to:

$$\varrho(\vec{r}) = \frac{1}{(2\pi)^3} \int \mathcal{A}(\vec{Q})\, e^{i\vec{Q}\cdot\vec{r}}\, d^3Q. \tag{3.5}$$

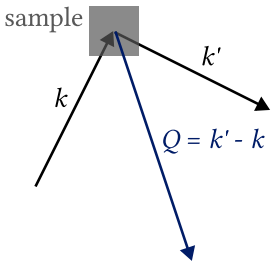

Figure 3.2: The scattering vector $\vec{Q}$ is visualised.

However, the problem is that in diffraction experiments the observed quantity is only the *scattering intensity* $\mathcal{I}(\vec{Q})$ and not the scattering amplitude $\mathcal{A}(\vec{Q})$. As can be seen in equation (3.13), the information which contains the phase difference of the scattered waves is lost.

3.2.1 Transformation to reciprocal space

The Fourier series of $\varrho(\vec{r})$ is:

$$\varrho(\vec{r}) = \sum_{h,k,l} \varrho_{hkl}\, e^{i\vec{G}_{hkl}\cdot\vec{r}} \qquad h,k,l \in \mathbb{Z}. \tag{3.6}$$

Since $\varrho(\vec{r})$ is looked at in three dimensions, h, k, l are three independent numbers called *Miller indices*. The Fourier coefficients are given by:

$$\varrho_{hkl} = \frac{1}{V_c} \int_{V_c} \varrho(\vec{r})\, e^{i\vec{G}_{hkl}\cdot\vec{r}} dV. \tag{3.7}$$

V_c is the volume of the unit cell and $\vec{G}_{hkl}$ is a *reciprocal lattice vector* of the form:

$$\vec{G}_{hkl} = h\vec{b}_1 + k\vec{b}_2 + l\vec{b}_3. \tag{3.8}$$

The relation between ϱ_{hkl} and $\vec{G}_{hkl}$ is bijective, i.e. every reciprocal lattice vector $\vec{G}_{hkl}$ is assigned to exactly one Fourier coefficient ϱ_{hkl} and vice versa. In analogy to the equation (3.2), the vectors $\vec{b}_1, \vec{b}_2, \vec{b}_3$ create a new coordinate system. Since h, k, l are discrete, every vector $\vec{G}_{hkl}$ represents one point of the *reciprocal lattice*. The reciprocal lattice is the Fourier transform of the lattice in real space. A combination of the equation (3.3) and the equation (3.6) and with the information that ϱ_{hkl} is independent of $\vec{r}$ yields:

$$\begin{aligned} e^{i\vec{G}_{hkl}\cdot\vec{r}} &= e^{i\vec{G}_{hkl}\cdot(\vec{r}+\vec{R})} \\ &= e^{i\vec{G}_{hkl}\cdot\vec{r}} \cdot e^{i\vec{G}_{hkl}\cdot\vec{R}} \\ &\Rightarrow e^{i\vec{G}_{hkl}\cdot\vec{R}} = 1 \\ &\Leftrightarrow \vec{G}_{hkl}\cdot\vec{R} = 2\pi n \qquad n \in \mathbb{Z}. \end{aligned}$$

From the equation (3.2) and the equation (3.8) therefore results:

$$\vec{b}_i \cdot \vec{a}_j = \delta_{ij}. \tag{3.9}$$

δ_{ij} is the Kronecker delta. The basis vectors of the crystal lattice in real space and the basis vectors of the reciprocal lattice are related by the following expression:

$$\vec{b}_1 = \frac{2\pi}{V_c}(\vec{a}_2 \times \vec{a}_3) \qquad \text{via cyclic permutation of the basis vectors} \tag{3.10}$$

and

$$(\vec{b}_1 \times \vec{b}_2)\cdot\vec{b}_3 = \frac{(2\pi)^3}{V_c}. \tag{3.11}$$

The vectors $\vec{b}_i$ have the dimension of an inverse length, which means that if the vectors $\vec{a}_i$ are reduced by a constant factor, the reciprocal lattice then expands by

this factor. This is why the corresponding space is called reciprocal space, k-space or momentum space ($p = \hbar k$). The *first Brillouin zone* is the Wigner-Seitz cell of the reciprocal lattice.

The plane in the crystal, spanned by lattice points, is called *lattice plane*. The indexing of those lattice planes is done by the Miller indices h, k, l. They are the inverse intercepts with the axis of the coordinate system. The index zero is selected for an intersection at infinity. This is shown in figure 3.3.

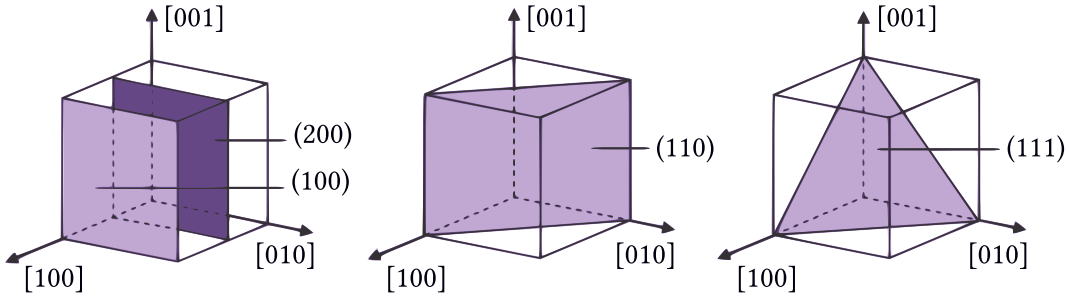

Figure 3.3: The Miller indices (hkl) are used to name the lattice planes, in this case of a cubic lattice. The name of the planes can be associated with the inverse intercepts with the axes. Source: Hunklinger [16].

The distance between the lattice planes is described by equation (3.12):

$$d_{hkl} = \frac{2\pi}{\left|\vec{G}_{hkl}\right|}. \tag{3.12}$$

The Miller indices can also be used to describe directions in real space. This is done with a notation in square brackets. In a cubic lattice, the direction $[hkl]$ stands perpendicular to the (hkl) plane. The $[hkl]$ direction is the same direction the reciprocal lattice vector $\vec{G}_{hkl}$ points to. This also implies that $\vec{G}_{hkl}$ stands perpendicular to the (hkl) lattice plane. If one of the Miller indices is negative, this is notated with a dash above the digit. Furthermore, in a hexagonal crystal lattice, it is common to introduce a fourth Miller index $i = -(h+k)$, which means a plane is thus named $(hkil)$. This is done to capture the three in-plane basis vectors $\vec{a}_i$ and the out-of-plane basis vector $\vec{c}$, as illustrated in figure 3.4. Now the question could be asked why one should introduce an extra index that contains no new information. This becomes evident when one tries to write the $[11\bar{2}0]$ direction, but with three cubic basis vectors. Note that you can *not* just leave out the index i, because the $(11\bar{2}0)$ plane from the hcp lattice is *not* the (110) plane shown in figure 3.3 of the cubic lattice.

Instead, one has to consider that the basis vectors of the cubic lattice are all orthogonal, while the vectors $\vec{a}_i$ of the hcp lattice are offset from each other by an angle of 120°. This means that two of the three orthogonal axis of the cubic system can be aligned with one a-axis and the c-axis of the hcp lattice structure. The remaining axis of the cubic system is offset by 30° from the remaining hcp axis. The conversion of the $[11\bar{2}0]$ direction in the hcp basis system into a system with cubic basis vectors would yield the $[1 \cos(30°) 0]$ direction. Having non integer Miller indices is inconvenient, which is why four indices are used to describe the hcp lattice.

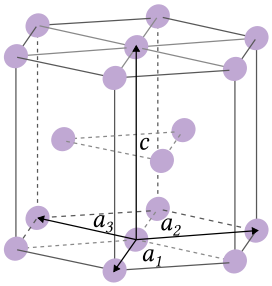

Figure 3.4: The hcp lattice structure has four basis vectors.

3.2.2 The von Laue condition

The scattering intensity $\mathcal{I}(\vec{Q})$ is proportional to the square of the scattering amplitude $\mathcal{A}(\vec{Q})$. Together with equation (3.4) one obtains the expression:

$$\mathcal{I}(\vec{Q}) \sim \left|\mathcal{A}(\vec{Q})\right|^2 = \left|\int_{V_s} \varrho(\vec{r})\, e^{-i\vec{Q}\cdot\vec{r}} dV\right|^2. \tag{3.13}$$

When the relation from equation (3.6) for $\varrho(\vec{r})$ of the reciprocal lattice is inserted, that yields:

$$\left|\mathcal{A}(\vec{Q})\right|^2 = \left|\sum_{h,k,l} \varrho_{hkl} \int_{V_s} e^{i(\vec{G}-\vec{Q})\cdot\vec{r}} dV\right|^2. \tag{3.14}$$

Since the function

$$e^{i(\vec{G}-\vec{Q})\cdot\vec{r}} \tag{3.15}$$

oscillates, the contributions of the summation are averaged to zero. Excluded from this is the case of $\vec{Q} = \vec{G}$, as here the value of the integral is finite:

$$\int_{V_s} e^{i(\vec{G}-\vec{Q})\cdot\vec{r}} dV = \begin{cases} V_s & \text{, if } \vec{Q} = \vec{G} \\ \approx 0 & \text{, else} \end{cases}. \tag{3.16}$$

The interference of the scattered waves is constructive in the case of $\vec{Q} = \vec{G}$. This observation condition is called the *von Laue condition*. The von Laue condition is visualised in figure 3.5.

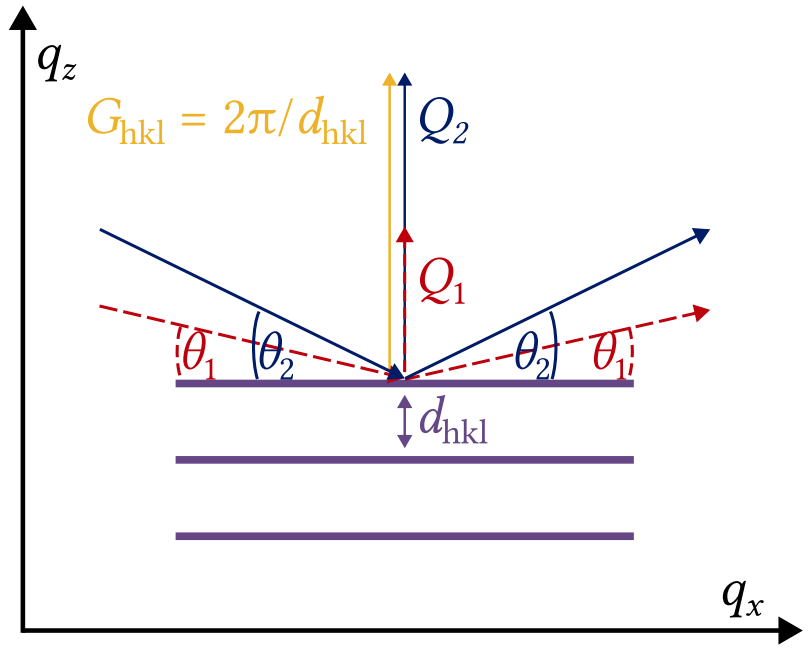

Figure 3.5: The diffraction angles θ_i are adjusted to change the length of the scattering vectors $\vec{Q}_i$ to match the reciprocal lattice vector $\vec{G}_{hkl}$ to satisfy the von Laue condition.

Different diffraction angles θ and photon energies, which are represented by the length of the $\vec{k}$-vectors, yield different $\vec{Q}$-vectors, like $\vec{Q}_1$ and $\vec{Q}_2$ in figure 3.5 with θ_1 and θ_2 respectively. If the scattering vector $\vec{Q}$ matches the reciprocal lattice vector $\vec{G}$, which is the case for $\vec{Q}_2 = \vec{G}_{hkl}$ in figure 3.5, then the von Laue condition is satisfied. Hence, every point of the reciprocal lattice is a point in momentum space, whose corresponding scattering vector $\vec{Q}$ satisfies the von Laue condition. In a thin-film, the out-of-plane direction in reciprocal space refers to the q_z direction, while the q_x and q_y direction are in-plane. As the reciprocal lattice vector depends on the distance between the lattice planes d_{hkl} (equation (3.12)), the relative change of the out-of-plane lattice constant can be determined by identifying the positional change of $\vec{G}$ along q_z, which is done by measuring Δq_z. In the following, three alternative interpretations of the Laue condition will be presented, namely the relation to Bragg's law (theorem 3.1), the connection to the concept of the Brillouin zone (theorem 3.2) and the visualisation of the von Laue condition through Ewald's sphere (figure 3.6).

▶ **Theorem 3.1 (Relation between the von Laue condition and Bragg's law).**

Bragg's law is a special case of the von Laue condition, as it can be directly derived under certain conditions. Suppose that

1. The scattering is symmetric, which means the angles of the incoming and diffracted beams are equal. ($\theta = \theta'$)
2. The scattering is elastic, which means $\left|\vec{k}\right| = \left|\vec{k}'\right|$.
3. The scattering is coplanar, which means that the incoming beam, the scattered beam and the normal of the diffraction plane all lie in one plane.

Then

$$\begin{aligned}
\left|\vec{Q}\right| &= \left|\vec{k}' - \vec{k}\right| && \text{| using figure 3.6} \\
&= 2\left|\vec{k}\right| \sin(\theta) && \left|\, \left|\vec{k}\right| = \frac{2\pi}{\lambda},\ \vec{Q} = \vec{G} \right. \\
\Rightarrow \vec{G} &= 2\frac{2\pi}{\lambda} \sin(\theta) && \left|\, \left|\vec{G}_{hkl}\right| = \frac{2\pi}{d_{hkl}} \right. \\
\Rightarrow \lambda &= 2d_{hkl} \sin(\theta).
\end{aligned}$$

Higher orders can also interfere constructively with d_{hkl}/n. With $d_{hkl} = d$, this leads directly to Bragg's law.

$$n\lambda = 2d \sin(\theta) \qquad n \in \mathbb{N}. \tag{3.17}$$

◀

▶ **Theorem 3.2 (Alternative formulation of the von Laue condition).** The von Laue condition can be rewritten, which reveals an interesting connection to the concept of the Brillouin zone. This derivation is adapted from Gross & Marx [1].

$$\begin{aligned}
\vec{k}' &= \vec{k} + \vec{G} && \left|^2 \right. \\
\left|\vec{k}'\right|^2 &= \left|\vec{k}\right|^2 + 2\vec{k} \cdot \vec{G} + \left|\vec{G}\right|^2 && \left|\, \left|\vec{k}\right| = \left|\vec{k}'\right| \right. \\
0 &= 2\vec{k} \cdot \vec{G} + \left|\vec{G}\right|^2 \\
\vec{k} \cdot \vec{G} &= -\frac{\left|\vec{G}\right|^2}{2} && \left|\, : \left|\vec{G}\right| \right.
\end{aligned}$$

$$\frac{\vec{k}\cdot\vec{G}}{\left|\vec{G}\right|} = -\frac{\left|\vec{G}\right|^2}{2\left|\vec{G}\right|} \qquad \left|\hat{G} = \vec{G}/\left|\vec{G}\right|\right.$$
$$\Rightarrow \vec{k}\cdot\hat{G} = \frac{G}{2}.$$

◀

The projection of $\vec{k}$ onto $\hat{G}$ is exactly $G/2$. The Brillouin zone is constructed to cover the region around a lattice point, where all points are closer to it than to any other lattice point. Consequently, the Brillouin zone's edge lies halfway to neighbouring lattice points, which means every scattering vector from the centre to the edge fulfils the von Laue condition.

Another geometrical visualisation of the von Laue condition is achieved by *Ewald's sphere*, illustrated in figure 3.6. This sphere is constructed such, that the endpoint of $\vec{k}$ points to any point of the reciprocal lattice, such as the origin (000). The circle around the starting point of the vector $\vec{k}$ with the radius of $\left|\vec{k}\right|$ is called Ewald's sphere. The von Laue condition is satisfied, if Ewald's sphere touches a reciprocal lattice point, because in that case $\vec{Q} = \vec{G}$.

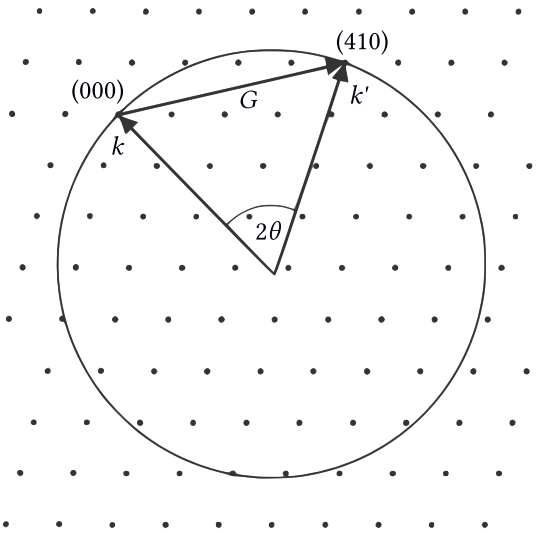

Figure 3.6: If the edge of Ewald's sphere touches a reciprocal lattice point, the von Laue condition is fulfilled. Source: Hunklinger [16]

3.3 Data acquisition routine

The fundamental concept in the determination of the lattice constant with X-ray diffraction (XRD) lies in the von Laue condition or Bragg's law, as described in section 3.2.2. The von Laue condition states that a diffraction peak, i.e. a local maximum of the diffracted intensity $\mathcal{I}(\vec{Q})$, can be observed if $\vec{Q} = \vec{G}$. When the distance between the lattice planes of a material is changed via a cryostat or laser excitation, the reciprocal lattice vector will change accordingly, as implied in equation (3.12). If the lattice expands, the absolute value of the reciprocal lattice vector will shrink. Consequently, the absolute value of the scattering vector has to shrink as well to satisfy the von Laue condition again. This can be achieved by either a reduced photon energy or a lower diffraction angle θ. Since the photon energy is not tunable at our setup, changing θ is the preferred method. The new diffraction angle which fulfils the von Laue condition corresponds to the new lattice constant. The same reasoning can be applied to Bragg' law, derived in theorem 3.1. Since the wavelength of the incident light is constant, $d \cdot \sin(\theta)$ has to stay constant in order to fulfil Bragg's law. A distance increase between the lattice planes must lead to a diffraction at lower angles θ, because $\theta \in [0, 90]$. The shift along the q_z direction of the peak shown in figure 3.7 is analysed with a Gaussian fit with linear background. This Gaussian fitted data is not the raw data collected by the detector. The detector images first need to be transformed into the reciprocal space.

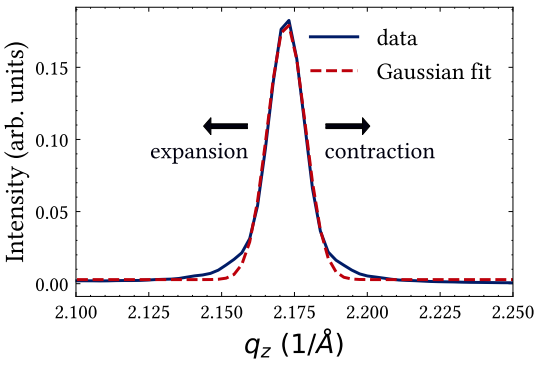

Figure 3.7: This exemplary Gaussian fit with linear background was taken for the Gd diffraction peak at 370 K.

3.3.1 Reciprocal space mapping

In a reciprocal space map (RSM), the scattered intensity $\mathcal{I}(\vec{Q})$ is assigned to each scattering vector $\vec{Q} = (q_x, q_y, q_z)$. In the context of thin-films samples, the diffraction peak can be assumed to be isotropic in q_x and q_y direction if symmetrical scattering is considered. This enables a projection of the three-dimensional peak on a two-dimensional map by the integration over the q_y direction. This two-dimensional map is depicted in figure 3.8. The raw images of the area detector show the scattered

X-rays. Each detector pixel measures the scattered intensity $\mathcal{I}(\theta)$, which is then transformed to a scattered intensity in reciprocal space $\mathcal{I}(\vec{Q})$. This numerical transformation process is described in more detail in the thesis of von Reppert [21].

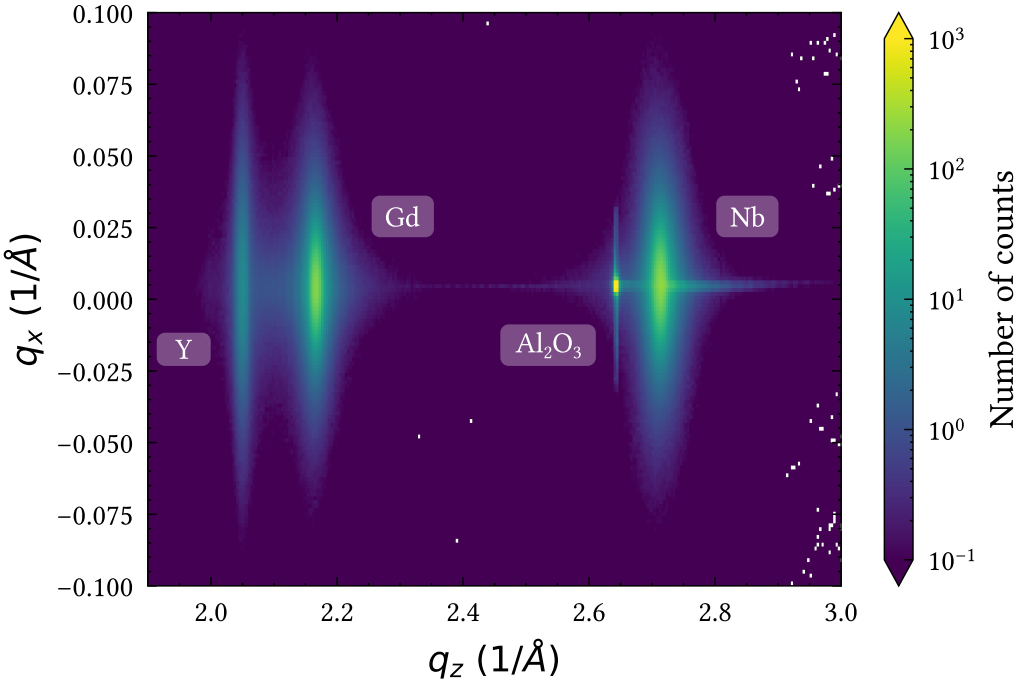

Figure 3.8: This is a RSM of the Gd sample shown in figure 2.1 (a) at 40 K. From left to right the peaks are Y, Gd, Al_2O_3 and Nb. For the Tb sample and the Dy sample, the Gd peak is replaced respectively. The peaks have a finite width in q_x, because the sample is neither a perfect single crystal nor infinity large. Consequently, the sharper nature of the Al_2O_3 substrate peak is due to its larger volume and indicates a high crystalline purity.

Each of the local diffraction intensity maxima (peak) can be associated with a lattice constant and thus a material of a sample from figure 2.1, because the peaks are located at material specific q_z positions, where the von Laue condition is fulfilled. When integrating a peak of the RSM from figure 3.8 over the q_x direction, one obtains a Gaussian peak as depicted in figure 3.7. A shift of this peak along the q_z-direction indicates a change of the out-of-plane lattice constant, which enables the measurement of the quasi-static or time-resolved strain. The concept of reciprocal space mapping is illustrated in figure 3.9. The incoming light with a wave vector $\vec{k}$ and an angle of incidence ω is diffracted on a sample. The outgoing light with the wave vector $\vec{k}'$ hits the detector, which is positioned under a detector angle

2θ. This type of scan is therefore called $\omega/2\theta$-scan. The condition $\omega = \theta$ defines a symmetric diffraction geometry.

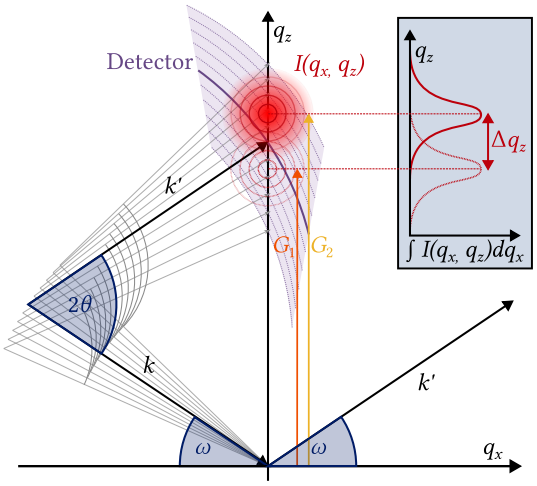

Figure 3.9: When a scan of a reciprocal space map is performed, the shift of the diffraction peak can be tracked by the adjustment of the angle of incidence ω and the detector angle 2θ. Note that opposing to the reciprocal space map in figure 3.8, the q_z-axis points upwards. Source: Zeuschner [22]

In figure 3.9, the light purple plane is a segment of the reciprocal space. The empty red circles indicate an old diffraction peak position, where the von Laue condition was satisfied for the lattice constant corresponding to the reciprocal lattice vector $\vec{G}_1$. The red filled circle indicates the diffraction peak which appears for a new lattice constant associated with $\vec{G}_2$. The intensity $\mathcal{I}(q_x, q_y)$ of the diffraction peak is measured by the detector for every angle of incidence ω. Therefore, each line on the light purple plane is a detector slice for a different ω and a segment of Ewald's sphere. The corresponding centre pixel of the detector lies on the q_z-axis. The angle of incidence ω can be varied to change the scattering vector and thus finding different diffraction peaks depending on the current reciprocal lattice vector of the analysed layer. A scan of a segment of the reciprocal space in this manner yields an $\mathcal{I}(\vec{Q})$ map, which is the reciprocal space map depicted in figure 3.8. The integration of the two-dimensional peak over the q_x direction leads to a Gaussian peak, as depicted in the blue inset in figure 3.9. The information of the change of the out-of-plane lattice constant is fully contained in Δq_z. As described in Zeuschner *et al.* [23], the change of q_z can be converted to a relative change of the out-of-plane lattice constant, which is called the strain η:

$$\eta = -\frac{\Delta q_z}{\left|\vec{G}\right| + \Delta q_z}. \tag{3.18}$$

Since Δq_z is on the order of 10^{-3}, the strain is practically proportional to Δq_z. The technique of reciprocal space mapping is important to evaluate the positions and widths of the diffraction peaks in reciprocal space. In some cases, a different technique for strain assessments can be used, which is called reciprocal space slicing. This technique is faster because the diffraction angle remains constant, which eliminates the need to record a detector image for each diffraction angle.

3.3.2 Reciprocal space slicing

The reciprocal space slicing (RSS), introduced in Zeuschner *et al.* [23], is a faster way to measure the shift of the diffraction peaks, as the diffraction angle ω is not changed during the experiment. The techniques of reciprocal space mapping and reciprocal space slicing are compared side by side in figure 3.10. When reciprocal space slicing is applied, only $\mathcal{I}(\vec{Q})$ of one detector slice is measured, which is the highlighted dark purple slice. This one-dimensional subset of the reciprocal space is a RSS. A RSM is composed of many RSS at different diffraction angles, which is illustrated as the light purple area in figure 3.10 (a). A change of the lattice constant of the material and thus the shift Δq_z of the diffraction peak in reciprocal space leads to the diffraction peak to slowly move out of the captured slice. However, it can still be measured, as the diffraction peaks have a finite width, because the sample is not infinitely large, has defects and the light used for the diffraction is neither monochromatic nor parallel. As the shifted diffraction peak does not lie in the centre of the detector slice any more, both a lower diffraction peak intensity and different position are recorded. This is indicated by the blue inset in figure 3.10 (b). In case of reciprocal space slicing, the measured shift $\Delta q_{z,\mathrm{D}}$ on the detector is not the same shift as Δq_z measured by reciprocal space mapping. The shift $\Delta q_{z,\mathrm{D}}$ has to be corrected to match the shift of the diffraction peak from centre to centre. This correction is called RSS correction.

Determination of the RSS correction factor

Depending on whether the RSM or RSS technique is used, a different shift of the diffraction peak in the q_z direction is determined. The correction of this discrepancy between $\Delta q_{z,\mathrm{D}}$ and Δq_z depends on the shape of the peak. The RSS factor S is

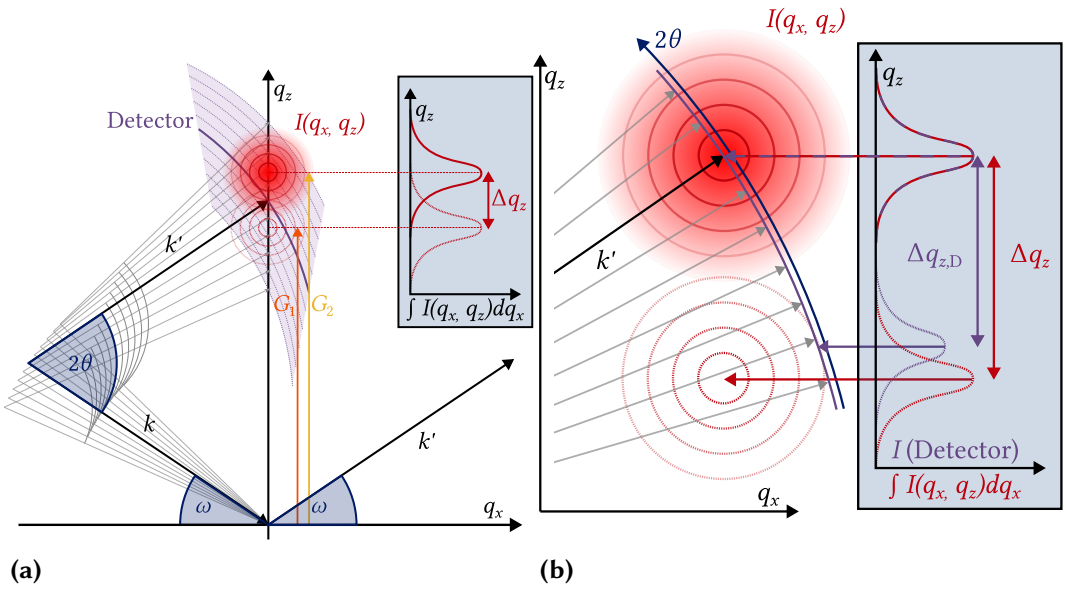

Figure 3.10: (a) Reciprocal space mapping: The diffraction peak moves down along the q_z direction, as the lattice expands. (b) Reciprocal space slicing: This causes the peak to shift out of the measured slice at a constant diffraction angle ω, but as it has a finite width, this slice is sufficient to observe a shift of the diffraction peak. However, the measured shift on the detector $\Delta q_{z,\mathrm{D}}$ is not the actual Δq_z. It has therefore be RSS corrected, depending on the shape of the diffraction peak and the diffraction angle. Source: Zeuschner [22]

calculated via equation (3.19), as described in Zeuschner *et al.* [23], under the assumption of a Gaussian peak shape.

$$S = 1 + \left(\frac{\sigma_z}{\sigma_x}\right)^2 \tan^2(\theta). \tag{3.19}$$

The RSS factor S depends on the widths σ_x and σ_z of the diffraction peak in the q_x and q_z directions, as well as the diffraction angle θ. Before the technique of reciprocal space slicing is applied, at least one RSM has to be recorded to determine the width of the diffraction peaks. In figure 3.11, the peak width of the rare-earth materials is shown as a function of temperature.

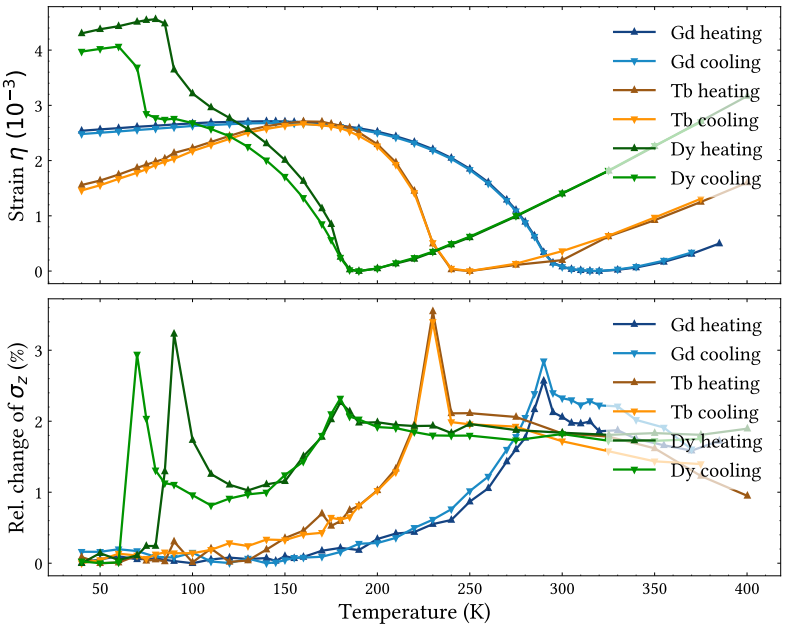

Figure 3.11: The diffraction peak width increases, while the material goes through a phase transition, which can be seen in the quasi-static strain measurements.

The comparison of the quasi-static strain measurements with the peak width σ_z (figure 3.11) reveals that the peak width increases at the phase transition temperatures, because the material does not transform homogeneously. The quasi-static strain measurements were conducted while the samples were heated (triangles pointing upwards) and cooled (triangles pointing downwards). The Dy sample has three local maxima in the width in the z-direction. The first two maxima at around 70 K and 90 K arise from the phase transition from ferromagnetic (FM) to helical antiferromagnetic (AFM) and back, as illustrated in figure 2.4. This phase transition

shows a hysteresis. The third peak in the peak width of the Dy sample occurs at roughly 180 K, where the material undergoes a second phase transition from AFM to paramagnetic (PM). The materials Gd and Tb only have this second phase transition from FM to PM at their respective Curie temperature. However, the relative change of the peak width is below 4%, rendering the temperature-resolved RSS factor practically constant, which is visualised in figure 3.12.

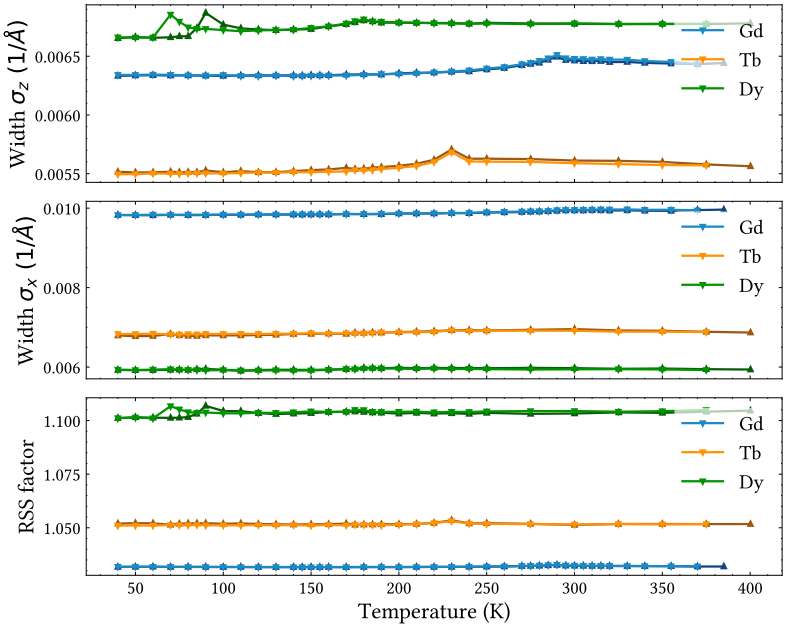

Figure 3.12: The temperature-resolved RSS factor was calculated by equation (3.19) and the use of the peak widths. The temperature-resolved RSS factor is practically constant, with small peaks around the phase transitions.

In order to calculate the transient, i.e. time-resolved RSS factor, the temperature-resolved average width σ_x of diffraction peaks are used. These widths are obtained by the technique of reciprocal space mapping. The time-resolved RSS factor $S(t)$ is calculated similarly to the constant RSS factor calculated in equation (3.19). As described in Zeuschner *et al.* [23], the width $\sigma_z(t)$ is now time-dependent:

$$\sigma_z(t) = \sqrt{\frac{\sigma_x^2 \sigma_\mathrm{D}(t)^2}{\sigma_x^2 - \sigma_\mathrm{D}(t)^2 \tan^2(\theta)}} \tag{3.20}$$

$$\Rightarrow S(t) = 1 + \left(\frac{\sigma_z(t)}{\sigma_x}\right)^2 \tan^2(\theta). \tag{3.21}$$

Here, $\sigma_D(t)$ is the transient width of the diffraction peak on the detector. An example of the time-resolved RSS factor is shown in figure 3.13.

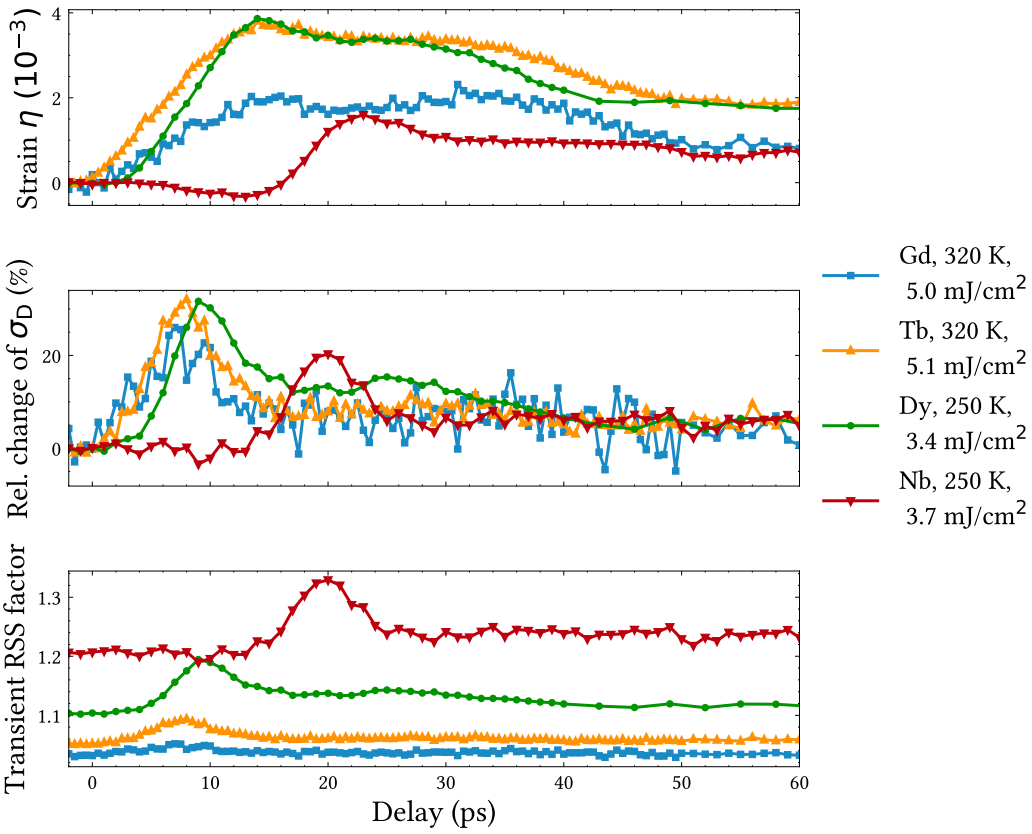

Figure 3.13: The transient RSS factor increases when the material shows an uncorrected strain. The transient RSS factor significantly influences the strain, with a change of up to 20%.

The time-resolved strain data was collected with the pump-probe setup outlined in section 5.1. The peak width $\sigma_D(t)$ on the detector and thus the transient RSS factor increases, when the material exhibits an inhomogeneous strain profile. As will be discussed in chapter 5, this is due to energy that flows into the respective layer, which includes a thermal expansion that does not homogeneously excite the layer and therefore broadens the peaks. In a first approximation, the transient RSS factor depends linearly on $\sigma_D(t)$, as can be seen in figure 3.13. The time-resolved RSS factor of Gd is almost constant in time, because the temperature-resolved RSS factor is close to one, since the diffraction peaks of Gd are the broadest in σ_x.

Part II

Experimental results

4 Extended Grüneisen model

This chapter presents the temperature-resolved quasi-static strain measurements of the Gd, Tb and Dy 40 nm thin-films carried out at the KMC-3 XPP endstation at BESSY II. The phononic and magnetic Grüneisen parameters of Gd, Tb and Dy are extracted in terms of an extended Grüneisen model. The extracted magnetic Grüneisen parameter is constant for Dy but surprisingly temperature-dependent for Gd and Tb. This result is unexpected, because previously conducted measurements at Dy and Ho ([3, 4]) have shown a temperature-independent Grüneisen parameter. The separation of the phononic and magnetic Grüneisen parameters is adapted from von Reppert et al. *[24].*

4.1 Endstation KMC-3 XPP at BESSY II

The endstation KMC-3 XPP at the BESSY II facility in Berlin, Adlershof is capable of time-resolved X-ray diffraction with tuneable photon energies in the hard X-ray regime. It is also well suited for temperature-resolved measurements of the quasi-static strain, because of its high brilliance. The time-resolution in the standard mode of operation of 100 ps is, however, often not sufficient to resolve ultrafast coherent strain dynamics, i.e. sound waves. For time-resolved ultrafast strain measurements, the plasma X-ray source was used, which is presented in chapter 5. The experimental setup of the KMC-3 XPP endstation at BESSY II is sketched in figure 4.1. The high brilliance synchrotron light source, the cryogenically cooled sample holder inside a vacuum chamber and the area pixel detector attached to a four-circle goniometer renders this setup optimal for the temperature-resolved strain assessments. The X-ray light is generated by highly relativistic electrons, which are deflected by a bending magnet. The thus generated synchrotron radiation is directed onto the sample via optical elements such as mirrors and a monochromator. The diffraction signal is then captured by the area detector. Further information about the experimental setup can be found in Rössle *et al.* [25]. At the KMC-3 XPP beamline, full reciprocal space maps (RSM) are recorded, which means that the reciprocal space slicing technique as described in section 3.3.2 is not utilised. An exemplary picture of an RSM can be found in figure 3.8.

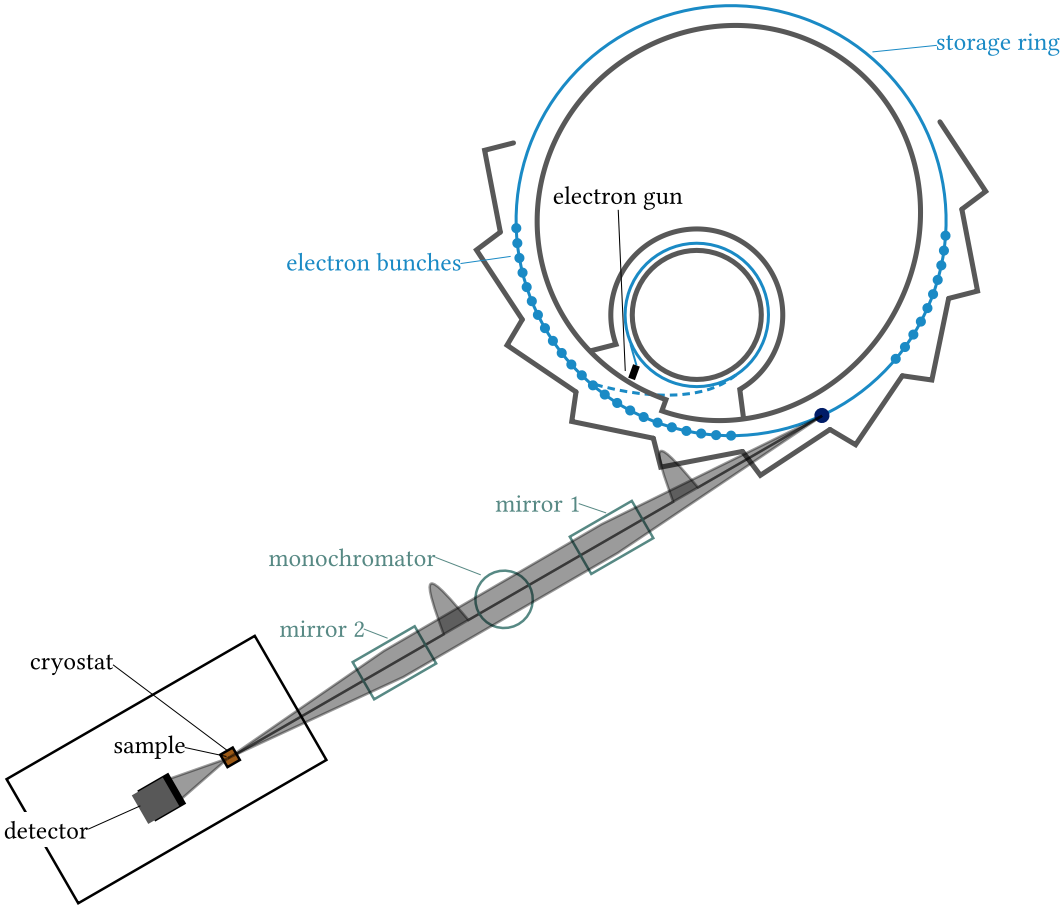

Figure 4.1: This is the experimental setup of the KMC-3 XPP beamline at BESSY II, reduced to the relevant components for static strain measurements. The figure is adapted from Rössle *et al.* [25]. The synchrotron light is directed onto the sample through X-ray optics. The sample can be cooled by a cryostat, and the resulting signal is captured by the detector mounted on a four-circle goniometer.

4.2 Temperature-induced static strain

The goal of the temperature-resolved strain measurements is to extract the phononic and magnetic Grüneisen parameters of Gd, Tb and Dy, which are required in order to understand and model the ultrafast strain dynamics. The magnetic Grüneisen parameter is the proportionality constant between the exerted magnetic stress and magnetic energy density in terms of an extended Grüneisen model presented in section 2.2.1. The first step to extract the Grüneisen parameter is to determine the temperature-resolved quasi-static strain (figure 4.2). Depending on the temperature, the strain can either be positive due to thermal expansion or negative, which is then called negative thermal expansion (NTE). The second ingredient necessary to extract the magnetic Grüneisen parameter is the heat capacity of each material (figure 4.3). The quasi-static strain is then converted to stress via equation (2.5), and the temperature is converted to a thermal energy density with equation (2.6). The stress and the energy density are subsequently divided into their electronic, phononic and magnetic components. The literature values and the extracted Grüneisen parameter can be found in table 4.1.

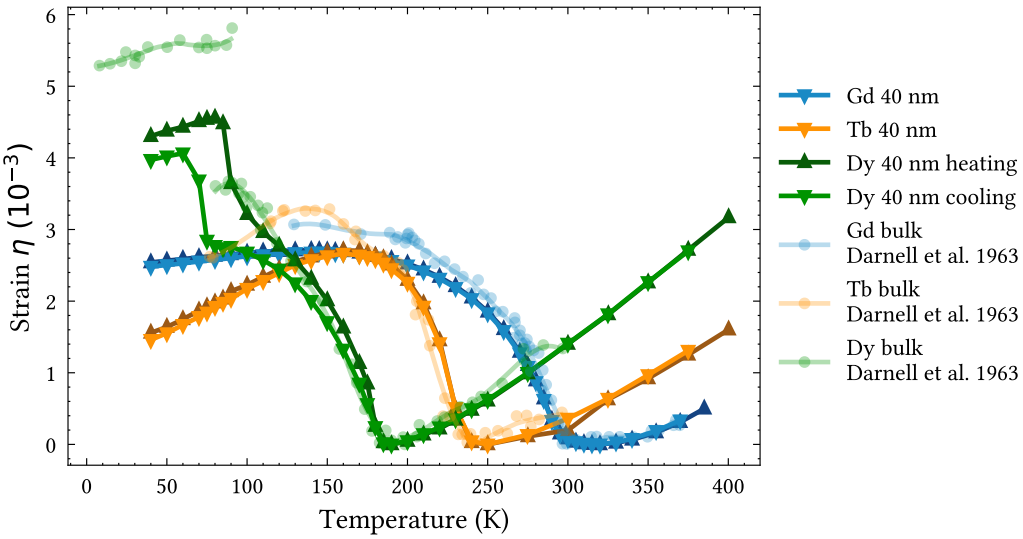

Figure 4.2: The measured temperature-resolved quasi-static strain of Gd, Tb and Dy is depicted with triangles pointing upwards while heated and with triangles pointing downwards while cooled. The quasi-static strain measurements for heating and cooling of Gd and Tb are practically identical, while Dy shows a hysteresis because of the additional phase transition into the AFM phase. The 40 nm thin-film data is also compared with bulk data (semi-transparent circles) from Darnell [26, 27].

The temperature-dependent shift of the diffraction peaks in the recorded RSMs at the KMC-3 XPP endstation are used to determine the strain of the rare-earth thin-films, as described in section 3.3. This strain is depicted in figure 4.2, together with the bulk data of the materials, which are nearly identical. The 40 nm rare-earth thin-film materials have in common that the linear thermal expansion (LTE) above their respective ordering temperature is driven by the phononic pressure. Despite the material is heated, a characteristic they also share is their contraction with a strain minimum at the magnetic ordering temperature. This contraction is called negative thermal expansion (NTE). For Gd and Tb, the ordering temperature is known as the Curie temperature, which is $T_{C,\,\mathrm{Gd}} = 320\,\mathrm{K}$ and $T_{C,\,\mathrm{Tb}} = 250\,\mathrm{K}$ in our samples respectively. For Dy, this ordering temperature is called the Néel temperature ($T_{N,\,\mathrm{Dy}} = 190\,\mathrm{K}$), since Dy already has gone through its ferromagnetic (FM) to helical antiferromagnetic (AFM) phase transition at lower temperatures. The magnetic ordering temperature corresponds to the minimum of an interpolated polynomial fit of the thin-film quasi-static strain data, which matches the bulk data. The temperatures found that way are roughly $20\,\mathrm{K} - 30\,\mathrm{K}$ higher than the respective literature values, which can be found in table 4.1. The reason for that discrepancy could be that the strain minimum is not aligned with the Curie temperature, as energy can still be deposited in the magnetic subsystem, even above the magnetic ordering temperature (Koç *et al.* [28]). The main difference of the temperature-dependent strain between Gd, Tb and Dy occurs 80 K below their respective magnetic ordering temperatures. The strain of Gd is mostly constant between 50 K 170 K. The strain of the Tb layer has a distinct maximum at around 170 K, while Dy goes through a second phase transition at approximately 80 K from FM to AFM, as illustrated in figure 2.4. In the FM phase of Dy, the heating and cooling measurements of Dy show a hysteresis. This different behaviour is also evident in the bulk material data from Darnell [26, 27]. However, a hysteresis is also visible in the AFM phase. In previous measurements (von Reppert *et al.* [4]), this hysteresis was not observed. The hysteresis in the AFM phase is likely an artefact caused by slight movements of the sample holder during heating and cooling. At the Curie temperatures of Gd and Tb and the Néel temperature of Dy, the lattice constants of the rare earths are minimal. Below these temperatures, the expensive phononic stress competes with a contractive stress induced by the magnetic subsystem. The idea of an extended Grüneisen model is to separate the stress components into a conventional positive phononic Grüneisen parameter and in our case a negative magnetic Grüneisen parameter.

4.3 Heat capacities of rare earths

The heat capacity is the next needed ingredient to determine the magnetic Grüneisen parameter. The measurements of the bulk heat capacity C_p at constant pressure from Griffel *et al.* [29], Jennings *et al.* [30], Griffel *et al.* [31] and Jennings *et al.* [32] for Gd, Tb, Dy and Lu are shown in figure 4.3.

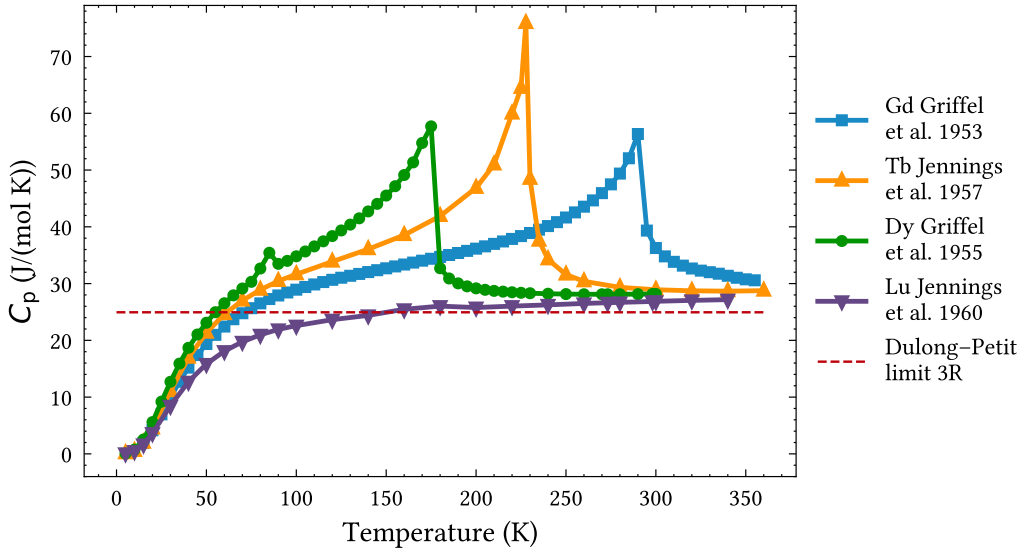

Figure 4.3: The temperatures where the peaks in the measured heat capacity data for Gd, Tb and Dy occur, can be identified as the phase transitions or magnetic ordering temperatures. The heat capacity of Lu is included as a proof of principle to illustrate the convergence against the Dulong–Petit limit of $3R$, indicated by the red dashed line.

The total heat capacity in figure 4.3 is the sum of the heat capacity of the electronic, phononic and magnetic subsystem, as illustrated in figure 2.6. All the materials have a higher heat capacity than predicted by the Dulong-Petit limit, which is partially because energy can still be distributed into the magnetic subsystem, even above the magnetic ordering temperature. Another contribution is the electronic heat capacity shown in figure 2.7 (a), which causes a deviation from the Dulong-Petit limit. This is supported by the heat capacity measurements of the paramagnetic rare-earth material Lu, which is included as a proof of principle, because the magnetic subsystem has no contribution to the heat capacity in this material. The measured data for Lu should therefore equal the sum of electronic and phononic heat capacities, as depicted in figure 2.7 (a) and figure 2.8 (a) respectively. The subtraction of those two heat capacities from the total heat capacity yields the magnetic part

of the heat capacity, which is shown in figure 2.9 (a). The corresponding energy density to the heat capacity of each subsystem is obtained by the integration of the heat capacity over the temperature (equation (2.6)). The data obtained in this way are interpolated and not measured, which is why they are not depicted with data points any more. As expected, the magnetic subsystem has almost no contribution in Lu for the heat capacity. The small but non-zero contributions arise because the literature value of the Debye temperature does not perfectly match the measurement values. The shape of the temperature-dependent heat capacity in Gd, Tb and Dy resembles the prediction from figure 2.10 well. The achieved result is that an energy density can now be assigned to each of the three subsystems at each temperature. The use of newer heat capacity data as in Dan'kov *et al.* [33], Jayasuriya *et al.* [34] and Pecharsky *et al.* [35] yields a very similar result. From statistical mechanics, the magnetic energy density of Dy below the phase transition is expected to be the largest, because it has the largest total angular momentum quantum number J, which can be seen in table 2.1. The following relation applies to the entropy for systems with quantized angular momentum:

$$S = \frac{\Delta Q}{T} = N k_B \ln(2J + 1). \tag{4.1}$$

This is confirmed, as the relation $\rho_{\mathrm{Dy,\,mag}} > \rho_{\mathrm{Tb,\,mag}} > \rho_{\mathrm{Gd,\,mag}}$ holds below their phase transition temperature into the paramagnetic phase.

4.4 Transformation from strain to stress

The strain η from figure 4.2 is related to the stress σ via Hooke's law (equation (2.5)). c_{33} is the corresponding elastic constant, as described in Gross & Marx [1]. This means that the temperature-resolved strain can be converted into a total temperature-resolved stress σ_{tot}, which is shown in figure 4.4 (a). The elastic constant c_{33} is assumed to be independent of the temperature, as its relative change is approximately 10% over the whole measured temperature interval. For more information on that, see the table of literature values table 4.1.

Figure 4.4 (a) depicts the stress plotted against the temperature, and figure 4.4 (b) shows the stress plotted against the phononic energy density. This is possible because figure 2.8 (b) relates each phononic energy density with a corresponding temperature. The phononic stress is then subtracted from the total stress to extract the magnetic Grüneisen parameter.

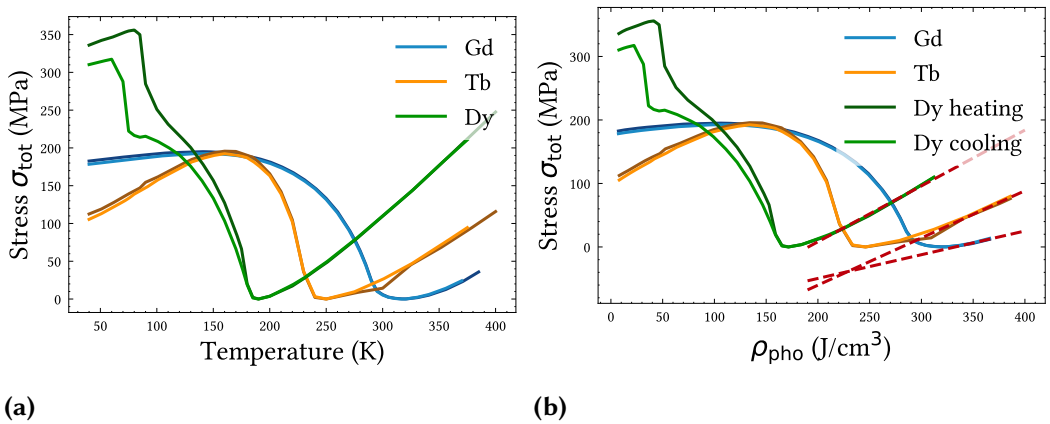

(a) **(b)**

Figure 4.4: (a) The total stress is plotted against the temperature. (b) The total stress is plotted against the phononic energy density corresponding to the measured temperature. The red dashed lines indicate the phononic contribution to the total stress, extracted from the high temperature limit.

4.5 Phononic and magnetic Grüneisen parameters

The Grüneisen model interprets the stress as an energy density, which can be seen in equation (4.2), since the Grüneisen parameter Γ is a dimensionless quantity.

$$\sigma = \Gamma \rho_E. \tag{4.2}$$

Applied to the phononic energy density, one can extract the phononic Grüneisen parameter Γ_{pho} as the slope of the red dashed lines in figure 4.4 (b), since the only present stress and therefore strain is exerted by phonons. The phononic Grüneisen parameters, extracted from the slopes of the linear functions in figure 4.5 (a), are $\Gamma_{\text{pho, Gd}} = 0.4$, $\Gamma_{\text{pho, Tb}} = 0.7$, $\Gamma_{\text{pho, Dy}} = 0.9$. As shown in figure 2.7 (b), the electronic energy density ρ_{ele} represents only a small fraction of the total energy density and can therefore be neglected. Those linear functions with the slope of the phononic Grüneisen parameter are plotted individually in figure 4.5 (a), and when they are subtracted from the total stress (figure 4.4 (b)), the remaining stress is the magnetic stress σ_{mag} (figure 4.5 (b)). The magnetic energy density ρ_{mag} can be calculated from the magnetic heat capacity, illustrated in figure 2.9 (b). In order to identify the magnetic Grüneisen parameters, one has to determine the slope of those functions. It stands out that the phononic Grüneisen parameter of Gd is much smaller than for Tb and Dy. The reason for this is presumably that the phononic expansion for Gd (red dashed line figure 4.4 (b)) is approximated linearly too close to the phase

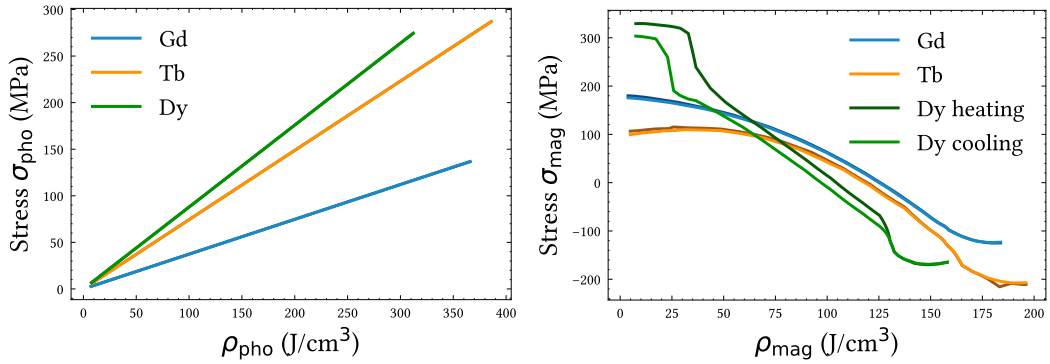

(a) **(b)**

Figure 4.5: The Grüneisen parameter can be identified as the slopes of the functions in the respective plots. (a) The phononic Grüneisen parameter is constant for Gd, Tb and Dy. (b) The magnetic Grüneisen parameter of Dy is constant, while it is energy density and therefore temperature-dependent for Gd and Tb.

transition of Gd. The use of high temperature literature values would probably lead to a steeper fit and a similar result compared to the other rare earths. By chance, the result of $\Gamma_{\text{pho, Gd}} = 0.4$ that I derived from my measured data up to 400 K agrees very well with the result in Koç *et al.* [28], where the Grüneisen parameter is calculated with equation (4.3).

$$\Gamma = \frac{\alpha B}{C_{\text{RE}}}. \tag{4.3}$$

Here, α is the linear thermal expansion, B the bulk modulus and C_{RE} the heat capacity of the rare-earth element. The bulk modulus assumes isotropic elastic constants, which do not apply to materials with an hcp lattice structure. This difference in the calculation explains the discrepancies that arise in the computation of the magnetic Grüneisen parameter compared to Koç *et al.* [28]. It is not possible to determine *one* magnetic Grüneisen parameter Γ_{mag}, as the slopes in figure 4.5 (b) are not constant any more.

4.5.1 Magnetic Grüneisen parameter of Gd

It is evident that the magnetic Grüneisen parameter of Gd is energy density and therefore temperature-dependent, since the slope of the graph of the function in figure 4.6 is not constant. However, it is still possible to determine two Grüneisen parameters, one for low and one for higher energy densities.

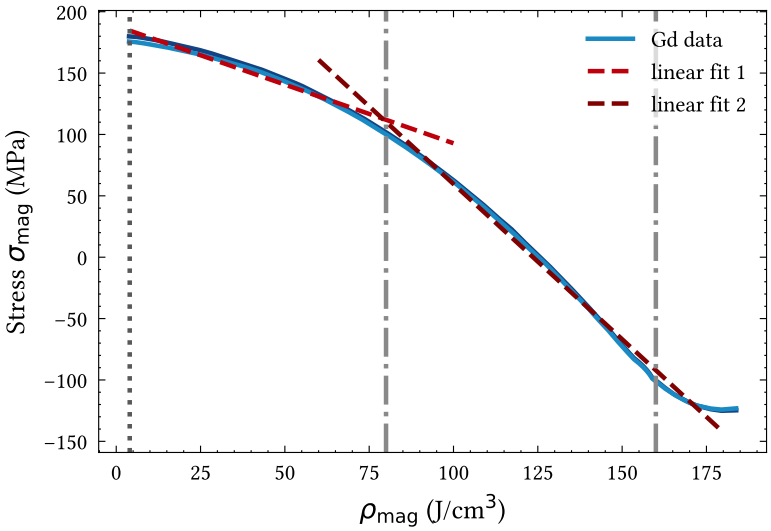

Figure 4.6: The extracted magnetic Grüneisen parameter of Gd is $\Gamma_{\text{mag, Gd}} = -2.5$, taken between 80 J/cm^3 (220 K starting temperature) and 160 J/cm^3 (320 K = $T_{C,\text{ Gd}}$). $\Gamma_{\text{mag, Gd}} = -1$ below the starting temperature.

The limit between those two regimes was chosen to be at 80 J/cm^3, which corresponds to a temperature of 220 K. This is exactly the temperature at which the time-resolved strain measurements in the ferromagnetic phase were conducted (see section 5.3.1), as it is 80 K below the phase transition. This qualifies that exact energy density as an appropriate starting point of the fit, because the determined Grüneisen parameter could then be used for the modelling of the time-resolved strain measurements in the FM phase. The other borders of the linear fits are the first data point at low energy densities and the measured Curie temperature of 320 K at high energy densities. The magnetic Grüneisen parameter of Gd, as determined by Koç *et al.* [28], ranges from $\Gamma_{\text{mag, Gd}} \in [-1, -2]$, which is of lower absolute value than the estimated $\Gamma_{\text{mag, Gd}} = -2.5$ presented here. Additionally, the possible underestimation of the phononic Grüneisen parameter would further increase the magnitude of $\Gamma_{\text{mag, Gd}} = -2.5$ and therefore further increase that discrepancy.

4.5.2 Magnetic Grüneisen parameter of Tb

Similar to the magnetic Grüneisen parameter of Gd, the magnetic Grüneisen parameter of Tb is not constant. It is practically zero at low temperatures, which is

counterintuitive, as it means that energy can be deposited in the magnetic system, but it does not exert any stress.

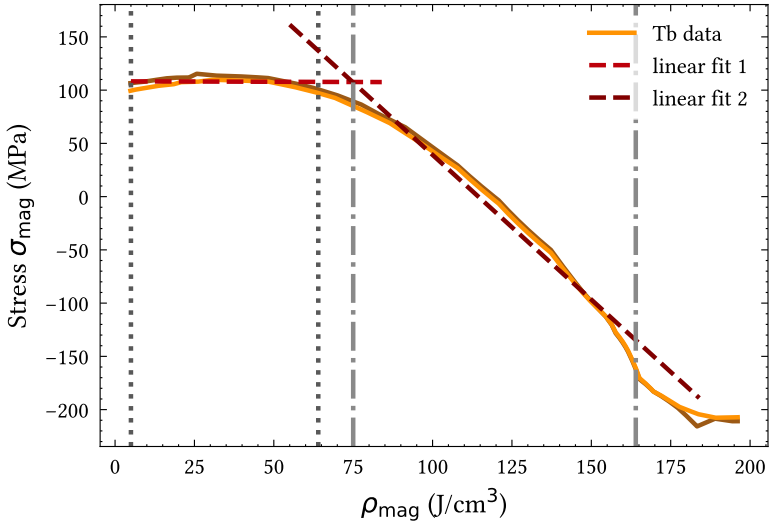

Figure 4.7: The extracted magnetic Grüneisen parameter of Tb is $\Gamma_{mag,\,Tb} = -2.7$. This linear fit 2 was taken between 75 J/cm^3 (170 K starting temperature) and 164 J/cm^3 (250 K = $T_{C,\,Tb}$). The constant regime of $\Gamma_{mag,\,Tb}$ is between 5 J/cm^3 (41 K) and 64 J/cm^3 (156 K).

The linear fit 1 in figure 4.7 was taken between the first data point and 64 J/cm^3 (170 K), as this is the range, where the approximation of a constant magnetic Grüneisen parameter is best. The lower boundary of the linear fit 2 is 75 J/cm^3, which corresponds to 170 K, which is again 80 K below the phase transition, where time-resolved measurements in the ferromagnetic phase were conducted (see section 5.3.2). The upper boundary is the measured Curie temperature of 250 K. If a Grüneisen parameter with higher accuracy is necessary, the use of more than two linear fits has to be considered, as the magnetic stress plotted against the magnetic energy density has a higher curvature for Tb than for Gd.

4.5.3 Magnetic Grüneisen parameter of Dy

The extraction of the magnetic Grüneisen parameter of Dy is more straight forward than for Gd and Tb, since it is approximately constant over the whole relevant temperature interval from 42 J/cm^3 to 130 J/cm^3. The lower boundary corresponds to 100 K, where the time-resolved strain measurements in the ferromagnetic phase were conducted (see section 5.3.3), and the upper boundary corresponds to the Néel temperature of Dy of 190 K.

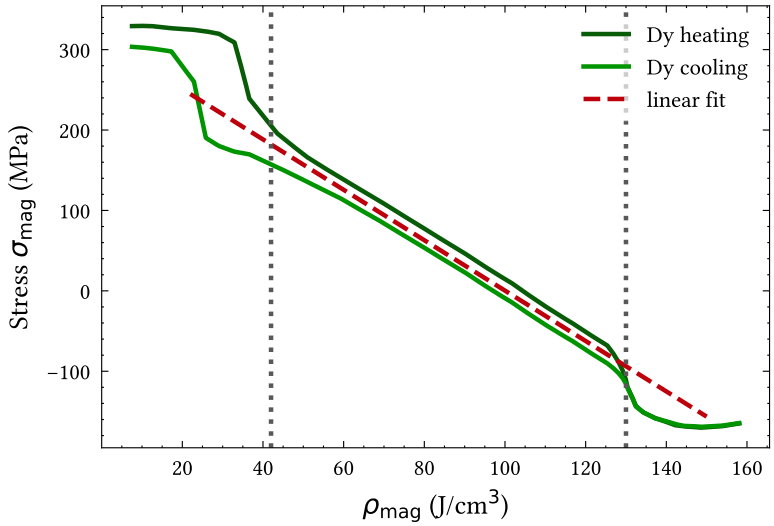

Figure 4.8: The extracted magnetic Grüneisen parameter of Dy is $\Gamma_{mag,\,Dy} = -3.1$. The linear fit was taken between 42 J/cm^3 (100 K starting temperature) and 130 J/cm^3 (190 K = $T_{N,\,Dy}$).

The hysteresis of the strain measurements presented in figure 4.2 is still visible during the phase transition into the AFM phase. This phase transition is most likely the reason why the heating and cooling Grüneisen parameter of Dy deviates but is perfectly aligned for Gd and Tb. The magnetic Grüneisen parameter for Dy, averaged over heating and cooling, amounts to $\Gamma_{mag,\,Dy} = -3.1$. This result agrees fairly well with the result from Mattern [36], where $\Gamma_{mag,\,Dy} = -2.9$ was determined. The constant nature of the magnetic Grüneisen parameter of Dy could be a coincidence, but similar results were found in measurements performed on Holmium in Pudell *et al.* [3], where the Grüneisen parameter of Holmium was also constant in temperature.

4.5.4 Comparison of Grüneisen parameters

It is still an open question why the magnetic Grüneisen parameter for Gd and Tb is temperature-dependent, while the magnetic Grüneisen parameter for Dy is constant. In a temperature interval where both Grüneisen parameters are non-zero, it applies that $|\Gamma_{mag}| > |\Gamma_{pho}|$, which can be seen in figure 4.9. This is the reason why Gd, Tb and Dy all exhibit a negative thermal expansion, which is also essential to understand the negative thermal expansion on ultrashort timescales presented in chapter 5.

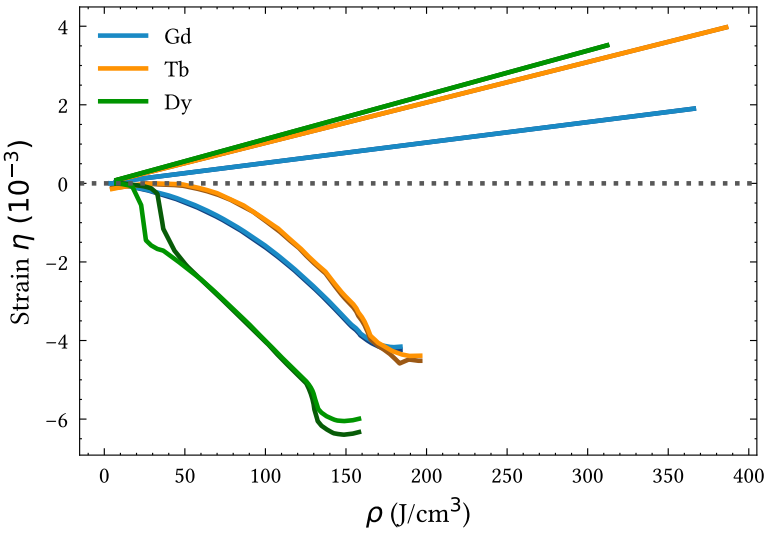

Figure 4.9: To get an overview of the magnitude of the phononic and magnetic Grüneisen parameters, they are here plotted in the same diagram against their respective energy density.

Table 4.1: The literature values for Gd, Tb, Dy and Lu are taken from Haynes [37], unless stated otherwise.

property	**Gd**	**Tb**	**Dy**	**Lu**
atomic weight (g/mol)	157.25	158.92534	162.50	174.967
density ρ (g/cm^{-3})	7.901	8.230	8.551	9.841
lin. therm. expansion c-axis α (10^{-6}/K)	10.0	12.4	15.6	20.0
Sommerfeld coefficient γ (mJ/(mol K^2))	4.48	3.71	4.9	8.194
bulk modulus B (GPa)	37.9	38.7	40.5	47.6
Debye temperature Θ_D (K)	182	177	183	185
elastic constant c_{33} at 298 K (GPa)[①]	71.9 [38]	72.25 [39]	78.1 [39]	/
measured mag. ordering temp. (K)	320	250	190	/
literature mag. ordering temp. (K)	294 [33]	220 [40]	179 [40]	/
phononic Grüneisen parameter Γ_{pho}	0.4	0.7	0.9	/
magnetic Grüneisen parameter Γ_{mag}	-2.5[②]	-2.7[②]	-3.1	/

[①] The elastic constants depend on the temperature, but the relative changes are rather small, e.g. for Tb, c_{33} at 80 K amounts to 79.83 GPa, which is roughly 1.1 times the value of c_{33} at 298 K. ([38, 39])
[②] The magnetic Grüneisen parameter for Gd and Tb are temperature-dependent. The given value is based on a linear fit between 220 K for Gd and 170 K for Tb and the corresponding Curie temperature.

5 Ultrafast magnetostriction

This chapter contains the time-resolved ultrafast strain measurements of Gd, Tb and Dy 40 nm thin-films carried out at the plasma X-ray source (PXS). I conducted the measurements on the Gd and Tb samples, while the measurements on the Dy sample were conducted by my colleagues Maximilian Mattern and Alexander von Reppert in 2021. Similar experiments have already been conducted in our group by Pudell et al. *[3] on Ho and by von Reppert* et al. *[4] on Dy with a different layer thickness. The time-resolved strain measurements of Gd by Koç* et al. *[28] at BESSY II were limited by a time-resolution of 100 ps, typical for synchrotron experiments. The thin-film strain responses are examined in two states, namely in the paramagnetic (PM) phase and in the ferromagnetic (FM) phase for Gd and Tb and in the antiferromagnetic (AFM) phase for Dy. The rare earths exhibit negative thermal expansion below their magnetic ordering temperature on a ps timescale. The laser-induced contraction of Gd is delayed, which indicates a slower demagnetisation compared to Tb and Dy. This result is in line with the findings of Wietstruk* et al. *[11]. The strain dynamics in the PM phase are unambiguously modelled by a one-energy and linear-chain-model with the udkm1Dsim toolbox, presented in Schick [41].*

5.1 Plasma X-ray source (PXS) setup

The plasma X-ray source (PXS) is a tabletop setup to generate femtosecond hard X-ray pulses with a kilohertz repetition rate. This is achieved by a focussed 50 fs (FMHM), 7 W and 1 kHz laser beam with a central wave length of 800 nm on a 15 µm thin copper tape. A copper plasma is created at the focal point, which leads to free electrons due to the high energy density. The free electrons are accelerated back to the copper, because of the oscillating electromagnetic field provided by the laser pulse, which consequentially leads to an emission of Bremsstrahlung and characteristic Cu-$K_{\alpha 1}$ and Cu-$K_{\alpha 2}$ radiation. The photons emitted from the Cu-$K_{\alpha 1,2}$ transitions have a wavelength of approximately $\lambda_{\text{X-ray}} = 1.54$ Å (8.047 keV and 8.028 keV [42]). They are then focused on the sample by a Montell X-ray optic with a divergence of 0.3°, which also acts as a monochromator, as described in Bargheer *et al.* [43]. The laser pulse with a central wavelength of 800 nm has a pulse duration of 50 fs. The generated X-ray pulse has a duration of < 250 fs, because

X-ray photons are only generated while energetic electrons with energies above 8 keV generated by the 800 nm laser pulse are present. The optical pump and X-ray probe pulses then hit the sample with a time delay Δt. The sample is mounted on a two circle goniometer together with a Pilatus X-ray area detector. A sketch of the PXS setup can be seen in figure 5.1. More detailed information about the PXS can be found in Zamponi *et al.* [14] and Schick *et al.* [15].

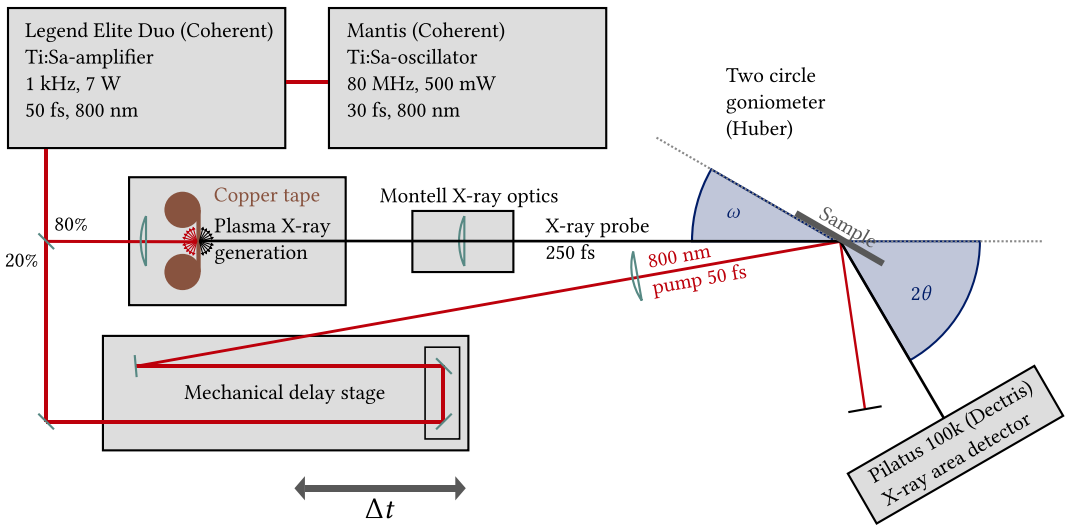

Figure 5.1: This sketch illustrates the PXS setup which, broken down to the essentials, is merely a pump-probe experiment with an 50 fs 800 nm pump and an 250 fs X-ray probe. The time delay Δt between pump and probe can be adjusted via the mechanical delay stage. The sketch is adapted from Zeuschner [22].

The laser pulses generated in the Ti:Sa-oscillator and Ti:Sa-amplifier of the company Coherent are split into two beams, which are used in this pump-probe experiment. The general concept of a pump-probe experiment is that the pump pulse excites (pumps) the sample. After the excitation, the probe pulse is used to analyse the sample, in our case to measure the Bragg-peak position and consequently the strain, utilising the von Laue condition introduced in section 3.2.2. It is common for pump-probe experiments to use optical pump and probe beams, but in order to diffract from the crystal lattice, an X-ray probe is necessary and used in a time-resolved XRD setup. Bragg's law reveals (theorem 3.1), that the wavelength has to be smaller than twice the distance of the lattice planes. Since the time delay Δt between the pump and probe pulse is variable, the temporal strain evolution can be evaluated (figure 5.2). In contrast to the measurements at the KMC-3 XPP endstation at BESSY II presented in chapter 4, the data acquisition routine used for my thesis at the

PXS involves reciprocal space slicing (RSS) as described in section 3.3.2, in order to reduce the measurement time. The data shown here is therefore RSS corrected by a time-resolved RSS factor.

5.2 Ultrafast strain dynamics in the paramagnetic phase

The time-resolved ultrafast strain dynamic measurements are started off with the investigation of the strain in the paramagnetic phase of the Gd, Tb and Dy thin-film samples, whose structure is shown in figure 2.1. In particular, each of the rare-earth samples contains a layer of the respective rare-earth material and a layer of Nb. The measured time-resolved strain (section 5.2.1) was modelled with a linear-chain-model (figure 2.11 (a)) and the one-energy-model (figure 2.6), to provide a sufficient understanding of the dynamics (section 5.2.2). The modelling of the ultrafast strain dynamics was carried out in the first 60 ps for each set of measurements.

5.2.1 Experimental strain transients

The experimentally determined strain transients of the rare-earth thin-films in the PM phase are depicted in figures 5.2 (a), 5.2 (c) and 5.2 (e). The corresponding signal of the Nb layer is shown in figures 5.2 (b), 5.2 (d) and 5.2 (f). The materials Gd, Tb and Dy all show positive strain due to thermal expansion, but only after 4 ps, as the Y layer on top is excited first. Similarly in all materials, this strain declines at delays above 120 ps, which can be interpreted as the heat that flows into the substrate of the sample. Before 120 ps, the strain dynamics are dominated by acoustic waves which propagate through the sample. Their impact on the strain can be visualised by a strain map, depicted in figure 5.3 (b).
The initial expansion during the first 10 ps is induced by the expansive strain wave that enters the rare-earth layer. At roughly 20 ps, a decline in the measured strain signal is observed across all rare-earth materials, because the strain wave partially exits the rare-earth layer and traverses to the underlying Nb layer. This is why the Nb layer shows its largest expansion at approximately 20 ps (figures 5.2 (b), 5.2 (d) and 5.2 (f)). A portion of the strain wave is reflected at the interface between the rare-earth material and the Nb. Since the reflected strain wave is lower in amplitude, a decline in the strain signal can be observed. When the strain wave hits the surface, i.e. the interface between Y and air, it is reflected into the sample again. As air has a larger acoustic impedance (slower sound velocity) compared to Y, the strain wave undergoes a phase shift of π, which transforms the reflected strain wave into

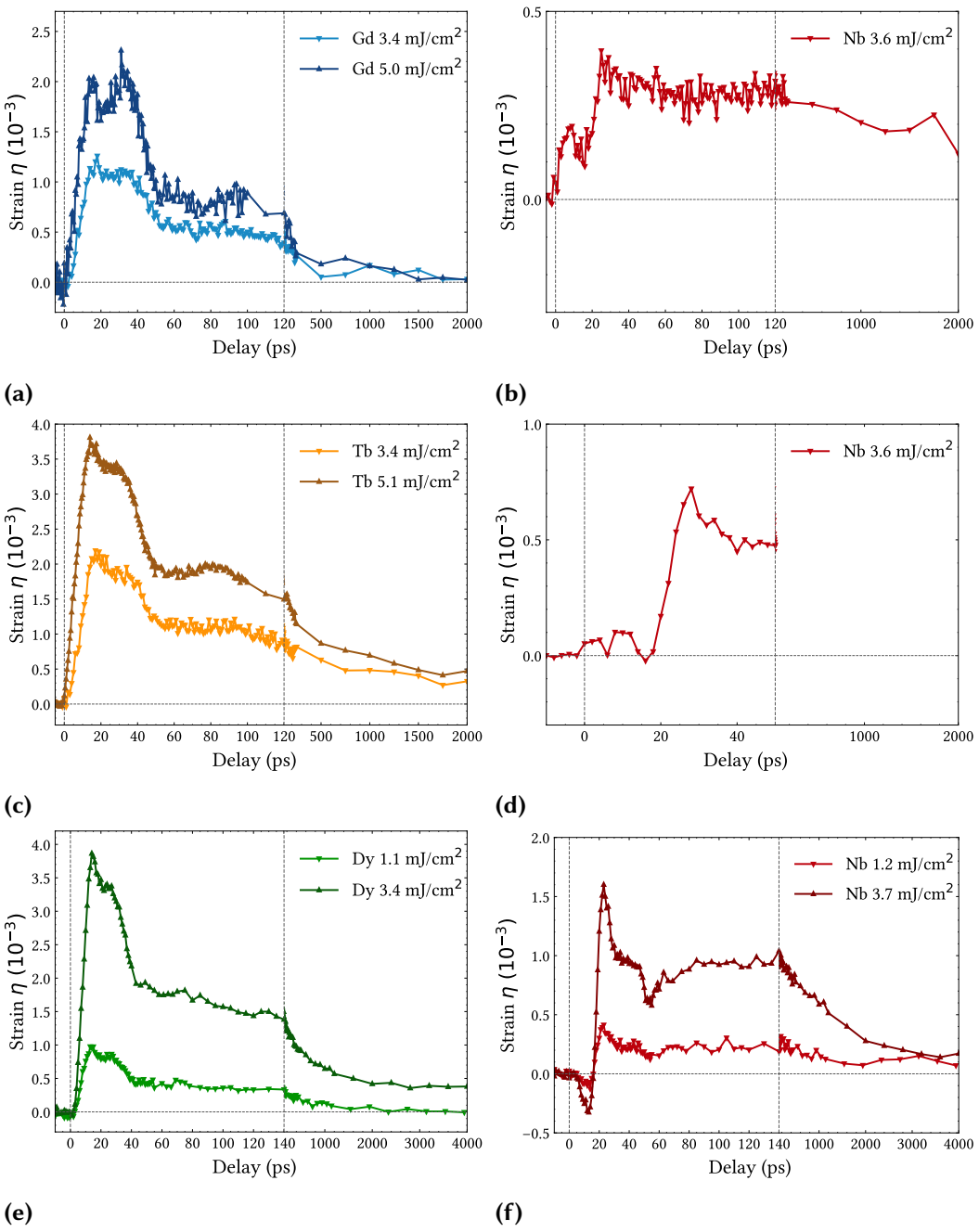

Figure 5.2: (a) shows the strain of the Gd layer at 320 K and (b) the corresponding Nb strain. (c) depicts the strain of the Tb layer at 320 K and (d) the corresponding Nb strain. (e) illustrates the strain of the Dy layer at 250 K and (f) the corresponding Nb strain.

the material to one of contractive stress. This is why the decay in the strain signal becomes steeper at around 40 ps. The shapes of transient strain maxima differ between the rare earths, most prominently at high fluences at 15 ps and 35 ps, as the strain of the Gd layer at 5.0 mJ/cm^2 shows two distinct maxima, while the second peak appears in the Tb and Dy layer only as a shoulder at 35 ps. The differences in the time-resolved shapes of the strain is supported by the simulation in section 5.2.2. The larger amplitude of Dy compared to Gd and Tb is also discussed there.

Since the rare earths are in their PM phase, no energy can be deposited in the magnetic subsystem of the three-energy-model illustrated in figure 2.6, because the spin system is already fully disordered. The excitation energy can only be deposited in the remaining electronic and phononic subsystems. Both exert a positive stress on the lattice, which leads to an expansion of the rare-earth materials after excitation. The main differences between the strain measurements in Gd, Tb and Dy are that Gd at 5.0 mJ/cm^2 shows far less strain than Tb at 5.1 mJ/cm^2. The strain of Dy at 3.4 mJ/cm^2 is about as large as of Tb at 5.1 mJ/cm^2 but at a significantly lower fluence. The observed strain of the Nb layer is severely impacted by the rare-earth layer above it, because an expansion of the rare-earth layer leads to a compression of the Nb layer. Since Dy exhibits the largest strain per fluence in the PM phase, the compression of Nb is most prominently visible in figure 5.2 (f). The thermal expansion of the Tb layer at 320 K is weaker than that of the Dy layer but stronger than of the Gd layer. Therefore, the thermal expansion of the Nb in the Tb sample induced by the laser excitation can be compensated by the contraction induced by the expansion of the Tb layer at timescales lower than 20 ps. The low strain amplitude of the Gd layer compared to the Tb and Dy layer can be explained by the fact that the measurement was conducted at 320 K where Gd is still close to its phase transition. The proximity to the Curie temperature enables some residual amount of energy to be distributed into the magnetic system, which counteracts the expansion since the magnetic Grüneisen parameter is negative, which was previously discussed in chapter 4. As a result, the Nb layer in the Gd sample shows an instantaneous expansion, because the compression of the Nb layer induced by the expansion of the Gd layer only hinders but not compensates the expansion induced by the laser excitation. The interpretations of these dynamics will now subsequently be verified with a one-energy and linear-chain-model.

5.2.2 Simulated strain transients

I used the udkm1Dsim toolbox by Schick [41] for the simulations, which is essentially based on a linear-chain-model as illustrated in figure 2.11. The length of the

red spacer sticks in this model is determined by the energy deposited in the sample by the pump pulse, which is calculated by a multilayer absorption model. Therefore, the first step is to generate a temperature map (figure 5.3 (a)), which defines the length of the spacer sticks for each time and sample depth. From that, a spatially and time-resolved strain map (figure 5.3 (b)) is generated, from which the average strain is calculated to fit the shape of the strain signal of the rare earths in the PM phase. The excitation fluence was used as a fit parameter. The simulations also act as a calibration for future simulations in the FM phase. The results of the simulation are depicted as a continuous line, while the measured data is shown as data points. Since thin-films are simulated, the Grüneisen parameters are Poisson corrected, as described in section 2.2.1. The literature values used for the simulations can be found in table 5.3.

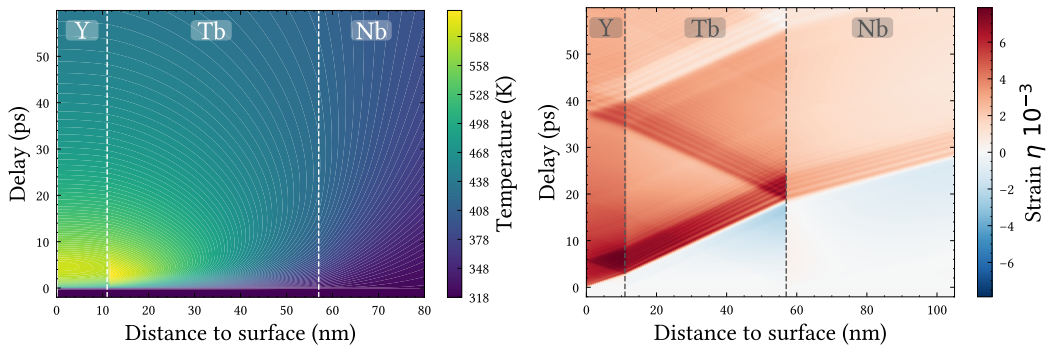

(a) **(b)**

Figure 5.3: The sample depth into the material is shown on the x-axis of these two figures, while the time delay is depicted on the y-axis. The two maps are plotted for the simulation condition of Tb at 4.4 mJ/cm^2. (a) The temperature map illustrates, that the surface of the sample directly after excitation is heated by roughly 300 K. The sample becomes colder towards the inside and it is cooling over time. (b) The strain map depicts the propagation of acoustic waves inside the sample.

Directly after excitation, the Tb layer is hotter than the Y layer, because it has a higher absorption, which is illustrated in figure 2.11 (b). Since the simulation is based on a one-temperature-model, the excitation of the Tb layer remains highly inhomogeneous, as hot electrons, which would contribute to a more homogeneous distribution of energy within the layer, are not taken into account.

Simulated strain transients of the Dy sample

The simulated transient strain of the Dy layer can be observed in figure 5.4. The initial expansion in the first 10 ps, driven by the strain wave which traverses the Dy layer, is well captured in both shape and amplitude. This is true for both excitation fluences of 1.1 mJ/cm^2 and 3.4 mJ/cm^2. The transition of the strain wave into the Nb layer is also visible as a decline in the strain signal at around 15 ps, as it is only partially reflected at the interface, which leads to a decline in the strain wave amplitude. Between 20 ps and 30 ps the strain signal stays roughly constant, as in this time span the reflected strain wave travels through the Dy layer with a constant amplitude. When the second reflection at the surface happens, the phase shifted reflected strain wave by π induces a contractive strain, that leads to a faster decay of the Dy strain signal, which can be observed at around 35 ps.

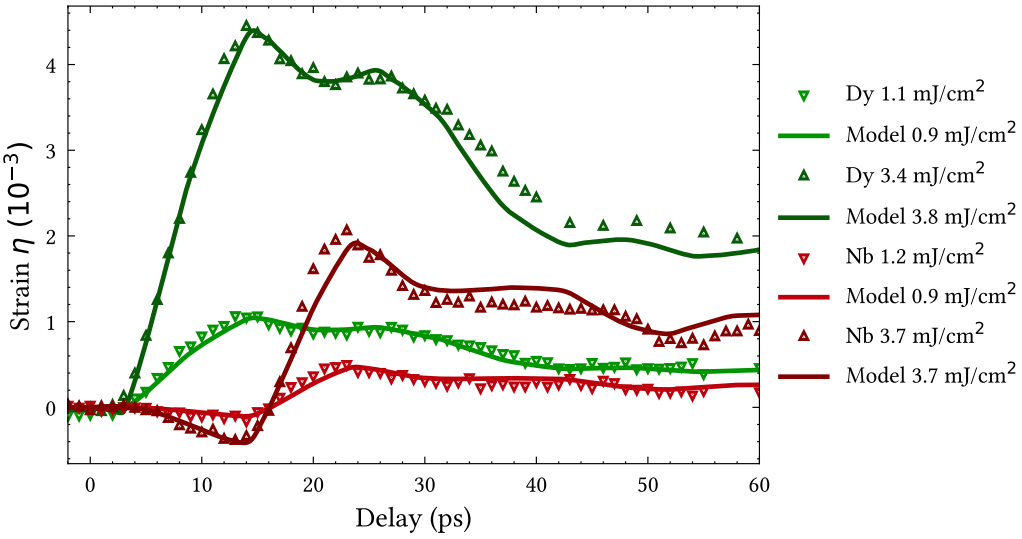

Figure 5.4: The strain amplitude and shape of the simulations of the Dy sample in the PM phase (continuous line) matches the measurements (data points) with a high accuracy.

The Nb layer expands at around 20 ps, which matches the timing of the strain wave that enters the Nb layer. A slight mismatch of the experimental data and the modelling can be observed at the strain transients of the 3.7 mJ/cm^2 Nb simulation. The minima of the strain waves perfectly overlap, while the maxima are offset by a few ps, which indicates that the literature sound velocity used for modelling is slower than the measured sound velocity.

Simulated strain transients of the Tb sample

The strain of the Tb layer and the Nb layer of the Tb sample, depicted in figure 5.5, show a similar behaviour to that of the Dy sample. The initial expansion of the Tb layer followed by the decline in strain wave amplitude, as well as the expansion of the Nb layer at 20 ps, is also prominent in the Tb sample. The timings of the strain maxima of the Tb signal are approximately 5 ps later than at the Dy signal. This is because the Dy sample is thinner, which can be seen in table 5.1. Tb and Dy have almost the same sound velocity which can be seen in table 5.3, as according to Graff [44], for a transversely isotropic material, the velocity of sound along the c-axis is given via $v = \sqrt{c_{33}/\rho}$. A more detailed discussion can be found in ROYER & Dieulesaint [45].

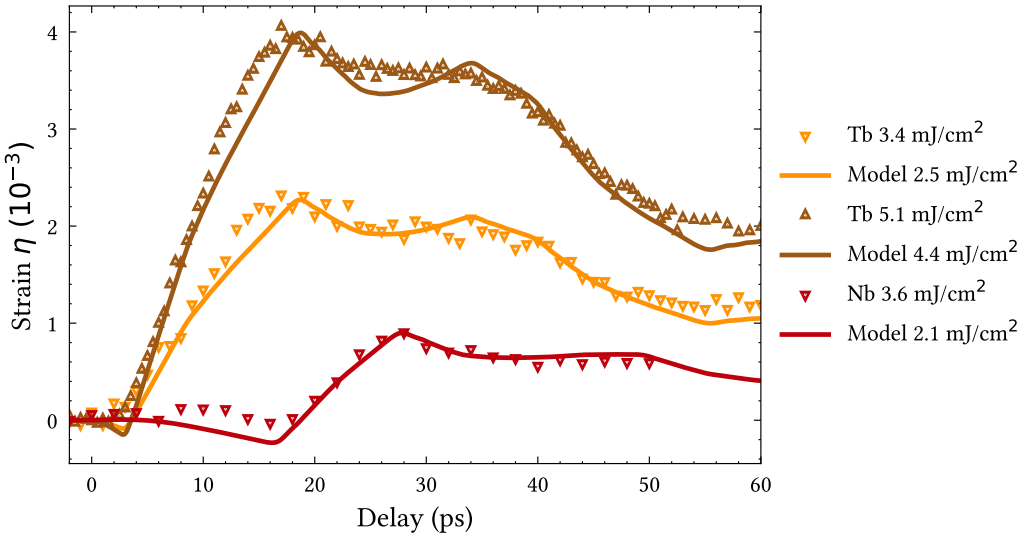

Figure 5.5: The shape of the simulations of the Tb sample in the PM phase (continuous line) matches the measurements (data points) well in both the Tb and Nb layer.

Compared to the Dy sample, the Tb sample has slightly more deviations between the transient strain measurements and the modelling. Especially in the modelling of the 4.4 mJ/cm^2, a second maximum becomes visible at 35 ps. This maximum is pronounced far less in the experimental data. Since the timing of the second maximum can be identified with the reflected strain wave shown in figure 5.3 (b) at the Tb-Nb interface which reaches the surface of the sample, one can assume this reflection to be less pronounced in the experiment compared to the simulation. The reason why the strain wave is not reflected perfectly at the interface may be

due to possible interface roughness or impurities, which would explain why the measured data show a less pronounced second strain maximum. Another deviation between the transient strain modelling and measurement is the fluence, which is estimated lower in the modelling than measured in the experiment. The phononic Grüneisen parameters of Tb and Dy are very similar, as depicted in figure 4.5 (a), which is why a similar transient strain would have been expected. This is why the simulations predict a larger expansion of every layer at the given fluence, which was not measured during the experiment. This lower expansion of the Tb layer could also explain the less pronounced compression of the Nb layer due to the overlying Tb layer earlier than 15 ps.

Simulated strain transients of the Gd sample

The qualitative behaviour of the transient strain of the Gd sample (figure 5.6) is in line with that of the Tb and Dy samples, as the same sound dynamics can be observed. A feature which was not present in the transient strain of the Tb and Dy samples is the pronounced second maximum of the transient strain in the Gd layer. This feature is also reproduced by the modelling.

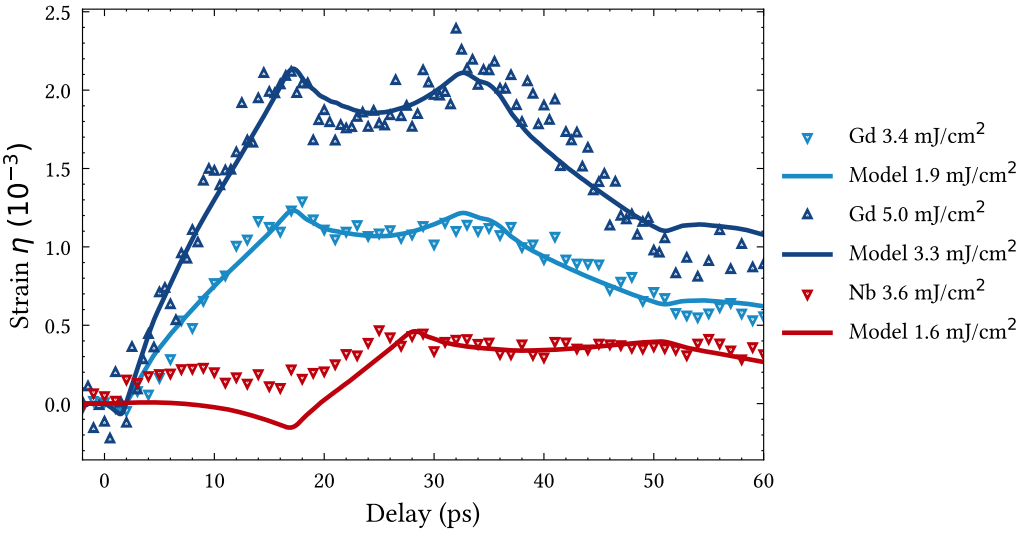

Figure 5.6: The shape of the simulations of the Gd sample in the PM phase (continuous line) matches the measurements (data points) well for the Gd layer but less well for the Nb layer.

The fluence of the simulations is far lower to achieve the same transient strain amplitude. The reason for that could be that the transient strain measurements

were conducted close to the magnetic ordering temperature of Gd. Consequently, energy can be deposited in the magnetic system which induces a negative thermal expansion, since the magnetic Grüneisen parameter of Gd is negative. Up to 25 ps, the shape of the Nb strain is not predicted very accurately by the model, as a weaker compression by the overlying Gd layer induces less pronounced sound dynamics in the Nb layer. It seems that the Nb is already heated after 5 ps, which would suggest a higher thermal conductivity of Gd compared to Tb and Dy. However, as shown in Koç [46], Gd has a lower thermal conductivity than Dy.

Fluence comparison of the transient strains

Now the question arises why the Dy layer shows a larger strain than the Gd and Tb layer normalised to the excitation fluence. According to table 5.3, the linear thermal expansion of Dy is larger than for Tb and Gd. This does not fully explain the observed behaviour, as the simulation already accounts for the larger linear thermal expansion of Dy. While the simulation fluences align well with the Dy measurements, they significantly underestimate the fluences of the Gd and Tb samples.

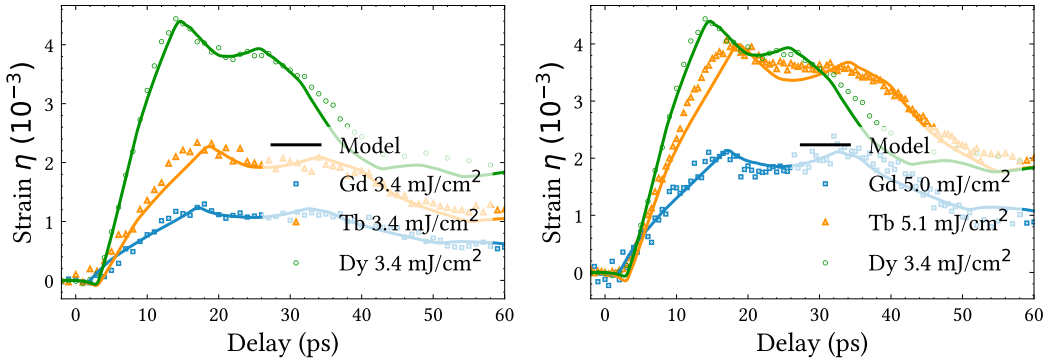

(a) **(b)**

Figure 5.7: (a) The measured strain amplitude of Dy is the largest at a fixed fluence of 3.4 mJ/cm^2, followed by Tb and the Gd. (b) The excitation fluence for Gd and Tb has to be increased to reach the strain amplitude Dy shows at a lower excitation fluence.

This indicates that the discrepancy in the strain amplitude between the samples is caused by an experimental error of the measurements of the Gd and Tb sample, e.g. a difference in fluence calibration. This is further supported by the fact, that also the Nb layers in the different samples show different strain amplitudes at large time delays for the same fluence, as already pointed out in figures 5.2 (b), 5.2 (d)

and 5.2 (f). When all strain waves have propagated to the substrate, the strain values should agree, since the Nb has the same linear thermal expansion in all three samples. The differences in the strain amplitude could also indicate that the Gd and Tb samples are oxidised, which could be why a higher fluence is necessary to achieve the same strain. This is supported by the fact that the same strain amplitude inconsistencies appear in the measurements of the ferromagnetic phase as well. Both sources of error are equally likely, because the measurements of the Dy sample were conducted 2 years before the measurements of the Gd and Tb sample and also the samples are of different age. Besides the inconsistencies of the strain amplitude, the shape of the strain is accurately captured by the simulations, which is shown in figure 5.7.

Simulation parameters

The parameters used for the simulations can be found in table 5.3. The interfaces between the layers of the sample are indicated as vertical dashed lines in figure 5.3. The simulations have revealed that the layer thicknesses given in figure 2.1 are not precise. The best simulation results were achieved with the layer thicknesses presented in table 5.1.

Table 5.1: This table contains the layer thickness provided by the simulations opposing to the layer thickness provided by the sample manufacturer.

layer	proposed thickness	simulated thickness
Gd sample		
Y	10 nm	8 nm
Gd	40 nm	44 nm
Nb	50 nm	54 nm
Tb sample		
Y	10 nm	9 nm
Gd	40 nm	43 nm
Nb	50 nm	54 nm
Dy sample		
Y	10 nm	10 nm
Gd	40 nm	36 nm
Nb	50 nm	49 nm

Another relevant fact which concerns the simulation parameters is the [110] orient-

ation of Nb. Since the toolbox is designed for 1D simulations, the elastic constants must be adjusted to match the proper propagation direction. For that, the elastic tensor C is changed in a way that it represents the elastic constants in the new coordinate system, defined by a coordinate transformation of the basis vectors, which corresponds to the [110] orientation. The old coordinate system consist of the standard Cartesian basis vectors, represented as E:

$$E = \begin{pmatrix} 1 & 0 & 0 \\ 0 & 1 & 0 \\ 0 & 0 & 1 \end{pmatrix}. \tag{5.1}$$

The new coordinate system, denoted by E_{new}, is chosen to align with the [110] direction, which is more convenient for the 1D simulation. It is defined by the following transformation matrix:

$$E_{\text{new}} = \begin{pmatrix} -\frac{1}{\sqrt{2}} & \frac{1}{\sqrt{2}} & 0 \\ 0 & 0 & 1 \\ \frac{1}{\sqrt{2}} & \frac{1}{\sqrt{2}} & 0 \end{pmatrix}. \tag{5.2}$$

In this new coordinate system one gets a new elastic tensor C_{new}, which entries can be used directly for the 1D simulations. The new values can be found in table 5.2.

Table 5.2: This table contains the elastic constants of Nb in the new coordinate system which align with the [110] direction.

c_{11} (GPa)	c_{12} (GPa)	c_{13} (GPa)	c_{33} (GPa)
221.45	138.7	138.7	221.45

5.3 Ultrafast negative thermal expansion in the ferromagnetic phase

The strain in the excited layer in the PM phase depends linearly on the fluence of the pump laser pulse, which is not the case on the FM phase. In order to understand the shape of the time-resolved strain of the rare earths in the FM phase, at least a two-energy-model is needed, which differentiates the energy in the magnetic subsystem from the energy in the electronic and phononic subsystem. Differences in the demagnetisation timescales have been observed in Wietstruk *et al.* [11], while Tb has the shortest, followed by Dy and then Gd. As discussed in section 5.2.2

for the PM phase, at nominally the same excitation fluence, both expansion and contraction in the Dy sample in the FM phase have larger absolute values than in the Gd and Tb sample. The time-resolved strain measurements in the FM phase were conducted 80 K below the magnetic ordering temperature of the respective rare-earth material.

5.3.1 Transient energy dynamics in Gd

The characteristics of the time-resolved strain in Gd cooled to 220 K (80 K below $T_{C,\,\mathrm{Gd}}$), shown in figure 5.8 (a), are highly fluence dependent. At 1.4 mJ/cm^2, no significant initial expansion is observed, but a contraction, which is smaller than for higher fluences. At 3.4 mJ/cm^2, an initial expansion can be identified, followed by a stronger contraction than at 1.4 mJ/cm^2. The initial expansion at 5.9 mJ/cm^2 is far more pronounced than for lower fluences, but the contraction does not get stronger by the same amount. This indicates that the magnetic system is near its saturation point, as no more energy can be deposited in the magnetic subsystem, since it is already fully disordered.

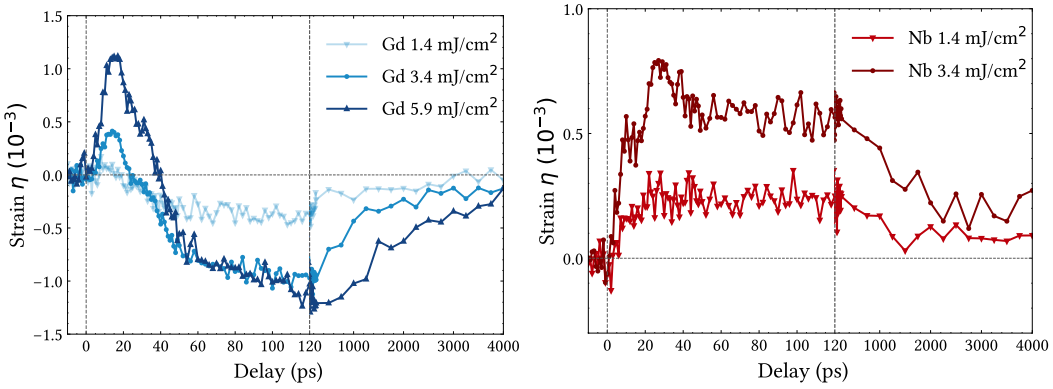

(a) (b)

Figure 5.8: (a) The fluence series of the time-resolved strain signal of the Gd layer in the ferromagnetic phase was measured at 220 K, which is approximately 80 K below the literature value of $T_{C,\,\mathrm{Gd}}$. (b) The Nb layer of the Gd sample shows positive strain.

The reason for the initial expansion at higher fluences is that more energy is deposited in the phononic than in the magnetic subsystem, which leads to a positive strain below 20 ps. Therefore, a one-energy-model cannot fully explain the observed behaviour of the strain of the Gd layer, as the ratio of the energy deposited by the laser in the phononic and magnetic subsystem changes with the initial

temperature and fluence. The excitation energy is transferred over time from the phononic subsystem into the magnetic subsystem. Additionally, the energy of the phononic system can be transferred into the substrate, which is not possible for the magnetic system (von Reppert *et al.* [24]). This non-equilibrium was previously observed by Koç *et al.* [28] and has now been measured with significantly higher temporal resolution. The measurement at 1.4 mJ/cm^2 shows no initial expansion, which indicates that the stress of the phononic and the stress of the magnetic system are nearly compensating each other. After 30 ps, however, a contraction can be observed, as the energy transport into the magnetic subsystem and the resulting demagnetisation takes place on at least two different timescales, which is in agreement with timescales measured in XMCD experiments on Gd by Wietstruk *et al.* [11]. The strain of the Nb layer, depicted in figure 5.8 (b), remains positive throughout the whole delay interval, as the expansion of the Gd layer does not significantly compress it. At a fluence of 5.9 mJ/cm^2, the Gd layer is expected to compress the Nb layer because of its higher strain amplitude. As in the PM phase, the positive strain in the Nb layer is driven by regular thermal expansion and is proportional to the excitation fluence.

5.3.2 Invar behaviour of Tb

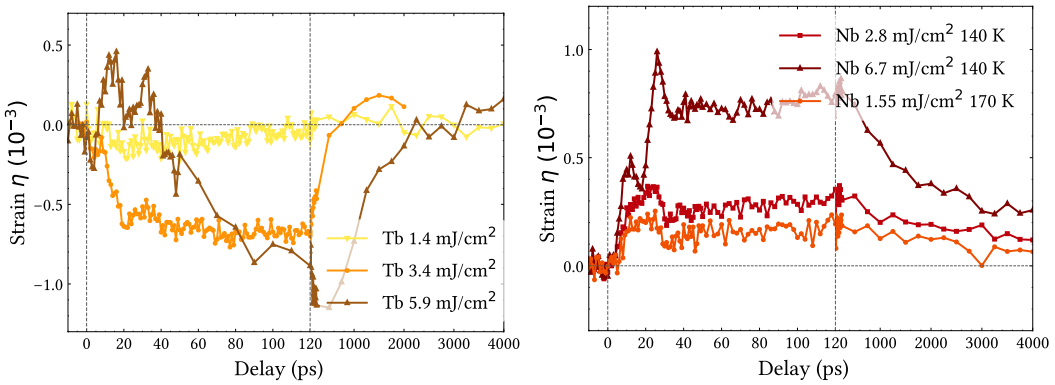

(a) **(b)**

Figure 5.9: (a) The fluence series of the time-resolved strain signal of the Tb layer in the ferromagnetic phase was measured at 140 K, which is approximately 80 K below the literature value of $T_{C,\,\mathrm{Tb}}$. (b) The Nb layer of the Tb sample shows positive strain at both 140 K and 170 K.

In contrast to the Gd layer, the strain of the Tb layer, measured 80 K below $T_{C,\,\mathrm{Tb}}$ (140 K) and shown in figure 5.9 (a), exhibits a less pronounced initial expansions,

even at high excitation fluences. This is due to the faster second demagnetisation timescale of Tb compared to Gd. It is also apparent that the magnetic system of Tb is not saturated when it is excited with 5.9 mJ/cm^2, because the contraction there is still much larger than at 3.4 mJ/cm^2. Interestingly, there is almost no contraction nor expansion at 1.4 mJ/cm^2, which is unexpected in such a time-resolved experiment, as the material shows an invar behaviour, i.e. minimal expansion or contraction after excitation. The reason for that is illustrated in figure 5.10.

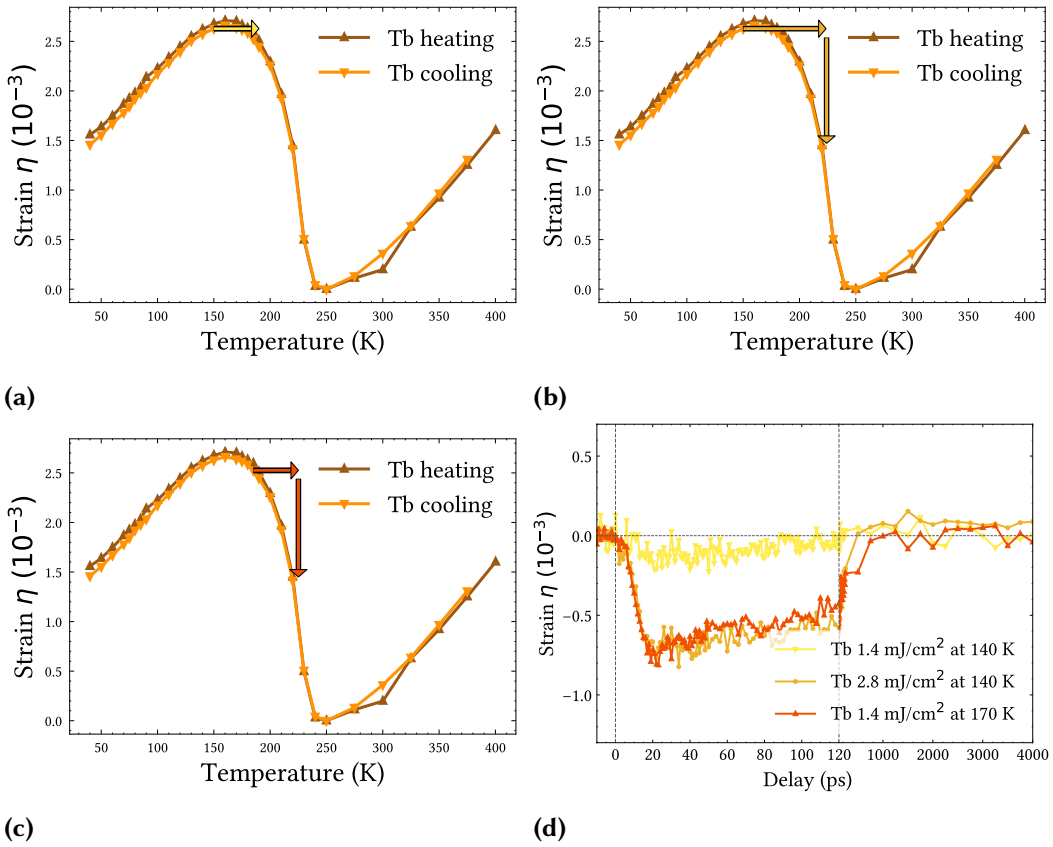

Figure 5.10: (a) The short horizontal yellow arrow at a starting position of 140 K indicates the excitation energy of 1.4 mJ/cm^2. This leads to almost no transient strain. (b) The long horizontal orange arrow indicates the excitation energy of 2.8 mJ/cm^2 with a starting position at 140 K. This leads to a transient strain of almost 1‰. (c) The same transient strain can be met with an excitation energy of 1.4 mJ/cm^2 starting at 170 K, indicated by the short red horizontal arrow. (d) Increasing the fluence or heating can therefore yield the same transient strain result!

The strain of the Nb layer of the Tb sample in figure 5.9 (b) behaves similarly to

the Nb layer of the Gd sample, as it expands after excitation. The excitation with 5.9 mJ/cm^2 is not enough to induce a compression of the Nb layer, because the initial expansion of the Tb layer is damped by the fast negative stress contribution of the magnetic subsystem. The measured time-resolved strain signals of the Tb layer for 2.8 mJ/cm^2 at 140 K and 1.4 mJ/cm^2 at 170 K are very similar. The quasi-static temperature-resolved strain measurements presented in the previous chapter 4 give a prediction on how strong the strain should change in equilibrium. Near equilibrium, every excitation fluence corresponds to a horizontal arrow length in the figures 5.10 (a) to 5.10 (c), because a higher excitation fluence would lead to more heating in the sample. In the case of figure 5.10 (a), no significant strain is expected, because the quasi-static strain at 140 K is very similar to the quasi-static strain at 170 K. When an excitation fluence of 1.4 mJ/cm^2 is identified with an average short term heating of 30 K, no significant strain in the time-resolved measurements is expected. This is exactly the case, as the strain at 1.4 mJ/cm^2 at 140 K shows very little strain. Following this line of reasoning, it should be possible to achieve the same strain result for a high fluence excitation at low temperatures and a low fluence excitation at higher temperatures, because the horizontal arrows end at the same spot. Exactly that is shown in figures 5.10 (b) and 5.10 (c). It is evident from figure 5.10 (a) that their strain is in fact very similar.

5.3.3 Magnetostriction in Dy

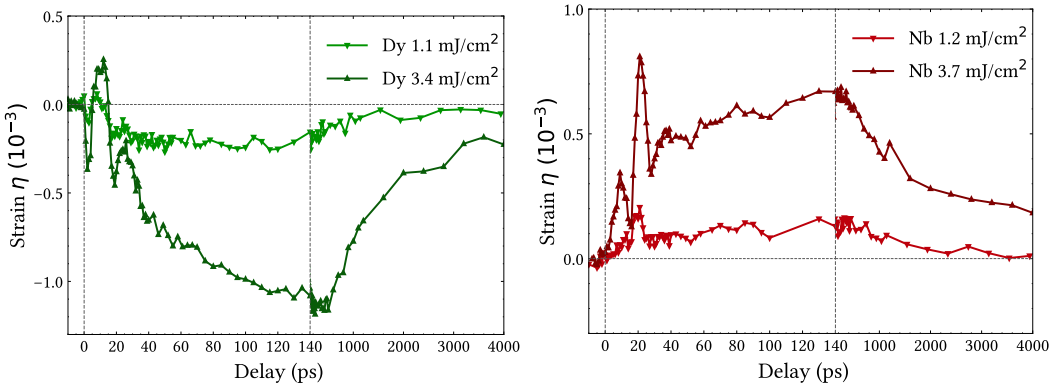

(a) (b)

Figure 5.11: The fluence series of the time-resolved strain signal of the Dy layer in the ferromagnetic phase was measured at 100 K, which is approximately 80 K below the literature value of $T_{N,\,\mathrm{Dy}}$. The Nb layer of the Dy sample shows positive strain.

The strain of the Dy layer 80 K below $T_{N,\,\mathrm{Dy}}$ (100 K), shown in figure 5.11 (a), is qualitatively similar to the strain of the Gd and Tb layer. The timescale of the demagnetisation in Dy seems to be in between of the of Gd and Tb, which is revealed by the comparison of the three materials at the same fluence in figure 5.12 (a).

5.3.4 Comparison of the demagnetisation timescales

The second timescales of demagnetisation can be well identified in figure 5.12 (a). The comparison of the measurements conducted at the same fluence of 3.4 mJ/cm^2, 80 K below the respective magnetic ordering temperature provides the result that the second demagnetisation in Tb is the fastest, followed by the Dy and then Gd. An increase in the fluence (see figure 5.12 (b)) shows that the largest fraction of the energy distributed into the magnetic subsystem occurs on the second timescale of demagnetisation. This results in NTE, as the magnetic Grüneisen parameter $|\Gamma_{\mathrm{mag}}| > |\Gamma_{\mathrm{pho}}|$. An initial expansion driven by the phononic subsystem is observed at high excitation fluences, as the second timescale of the demagnetisation only starts at approximately 15 ps.

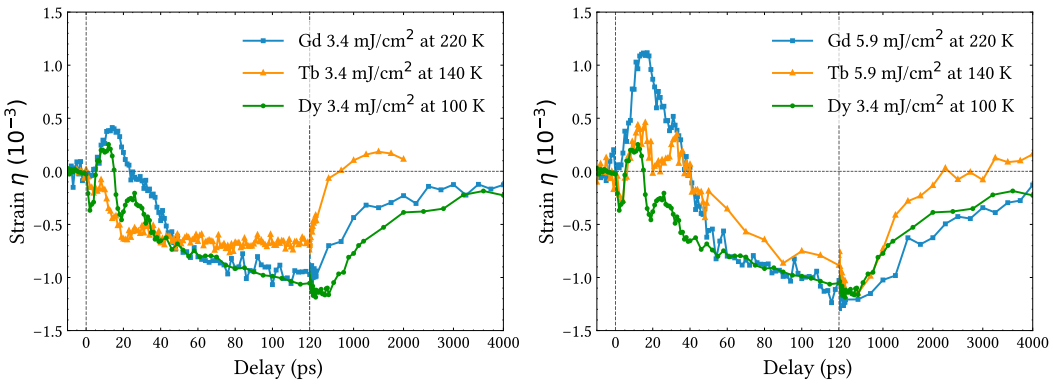

(a) **(b)**

Figure 5.12: (a) The comparison of the demagnetisation timescales of Gd, Tb and Dy at 3.4 mJ/cm^2 shows that Tb seems to have the shortest timescale of demagnetisation, followed by Dy and then Gd. (b) The larger initial expansion of the Gd layer at a higher fluence of 5.9 mJ/cm^2 also indicates that less energy is transferred into the magnetic subsystem.

The timescale of the demagnetisation in Tb is on the order of magnitude of 10 ps, while the demagnetisation of Dy is slower, with more than 20 ps. Gd has the slowest demagnetisation of these three rare-earth materials, with a timescale of around 50 ps. This is in agreement with the results of Wietstruk *et al.* [11], where a second demagnetisation timescale of 8 ps for Tb and 40 ps for Gd is estimated.

Table 5.3: The simulation parameters were taken from Haynes [37], unless stated otherwise.

property	Gd	Tb	Dy
crystal lattice structure	hcp	hcp	hcp
c-axis out-of-plane (Å)	5.7810	5.6966	5.6501
a-axis in-plane (Å)	3.6336	3.6055	3.5915
b-axis in-plane (Å)	3.6336	3.6055	3.5915
density ρ (g/cm^3)	7.901	8.230	8.551
lin. therm. expansion $\alpha_\perp$ (10^{-6}/K)	10.0	12.4	15.6
lin. therm. expansion $\alpha_\parallel$ (10^{-6}/K)	9.1	9.3	7.1
heat capacity c_p at 25 °C (J/(kg K))	236	182	173
therm. conductivity κ (W/(m K))[①]	10.8 [47]	14.8 [47]	11.7 [47]
refractive index $n + ik$	from [48]	from [48]	from [48]
n	1.99	2.36	2.68
k	3.30	3.21	3.21
elastic constants at 300 K (GPa)	from [38]	from [39]	from [39]
c_{13}	21.3	22.99	22.3
c_{33}	71.9	72.25	78.1

property	Y	Nb	Al_2O_3
crystal lattice structure	hcp	bcc [1]	hcp
c-axis out-of-plane (Å)	5.7318	4.67 [1]	12.9933 [49]
a-axis in-plane (Å)	3.6482	4.67 [1]	4.7602 [49]
b-axis in-plane (Å)	3.6482	3.30 [1]	4.7602 [49]
density ρ (g/cm^3)	4.469	8.57	3.97
lin. therm. expansion $\alpha_\perp$ (10^{-6}/K)	19.7	6.8 [50]	7.07 [51]
lin. therm. expansion $\alpha_\parallel$ (10^{-6}/K)	6.0	6.8 [50]	6.2 [51]
heat capacity c_p at 25 °C (J/(kg K))	298	265	657.22 [52]
therm. conductivity κ (W/(m K))[①]	24.8 [47]	53.7 [47]	58.33 [53]
refractive index $n + ik$	from [48]	from [48]	from [37]
n	2.10	2.15	1.76
k	2.67	3.37	0
elastic constants at 300 K (GPa)	from [54]	from [55]	from [56]
c_{13}	21	138.7	116
c_{33}	76.9	245.6	501

[①] All values were taken at 300 K, except for Yttrium, which was taken at 160 K.

6 Conclusions & outlook

Conclusion

Quasi-static and transient strain measurements at the thin-film rare-earth metals Gd, Tb and Dy have been conducted. The temperature-resolved strain measurements in the range of 50 K to 385 K were carried out at BESSY II utilising X-ray diffraction. It was shown that the thin-film rare-earth metals Gd, Tb and Dy exhibit negative thermal expansion below their magnetic ordering temperature. Quasi-static strain measurements allowed for the extraction of both phononic and magnetic Grüneisen parameters. The extracted magnetic Grüneisen parameter of Dy has a constant value of $\Gamma_{\mathrm{mag,\,Dy}} = -3.1$, while the value is temperature-dependent for Gd and Tb. For Gd, a magnetic Grüneisen of $\Gamma_{\mathrm{mag,\,Gd}} = -2.5$ was determined between 220 K and 320 K. The magnetic Grüneisen parameter of Tb is estimated to be $\Gamma_{\mathrm{mag,\,Tb}} = -2.7$ between 170 K and 220 K. These values are of slightly higher magnitude compared to Koç *et al.* [28], because I took the anisotropy of the elastic constants into account. If I adjusted the phononic Grüneisen parameter to the high temperature limit, this discrepancy would be amplified further.

I observed ultrafast time-resolved magnetostriction in thin-film rare-earth metals at our laboratory based plasma X-ray source and utilised the techniques of reciprocal space mapping and reciprocal space slicing, including a transient RSS correction. Picosecond strain dynamics and non-equilibrium energy transport on a nanosecond timescale have been determined via the transient strain measurements, which I also simulated with the udkm1Dsim toolbox (Schick [41]). I observed ultrafast NTE, 80 K below the magnetic ordering temperature of Gd, Tb and Dy. With the highest excitation fluences, the Gd layer showed a saturation of the magnetic subsystem, as no further energy could be deposited in the fully disordered spin system. In contrast, Tb showed no saturation and for Dy, no such measurements were conducted. The delayed laser-induced contraction of Gd indicates a slower demagnetisation compared to Tb and Dy. The demagnetisation timescale of Tb is around 10 ps, the demagnetisation timescale of Dy is slower than 20 ps, and the demagnetisation timescale of Gd is roughly 50 ps. Of special interest is the ultrafast invar behaviour of the strain of the Tb layer, under the condition of a certain excitation fluence and starting temperature. When the Tb layer is excited

with 2.8 mJ/cm^2 at a starting temperature of 140 K, it yields approximately the same strain as an excitation with 1.4 mJ/cm^2 at 170 K. If the Tb layer is excited with 1.4 mJ/cm^2 at 140 K, essentially zero expansion is measured, i.e. we observe an ultrafast invar effect, where the rare earth is heated, but the energy does not lead to any stress or strain.

Outlook

In addition to the quasi-static strain measurements presented in chapter 4, temperature-resolved strain measurements at the Gd and Tb layer were performed with an applied external 140 mT in-plane magnetic field. The magnetic field should raise the Curie temperatures of Gd and Tb, as the magnetic order can be maintained up to higher temperatures. The results of these measurements are depicted in figure 6.1

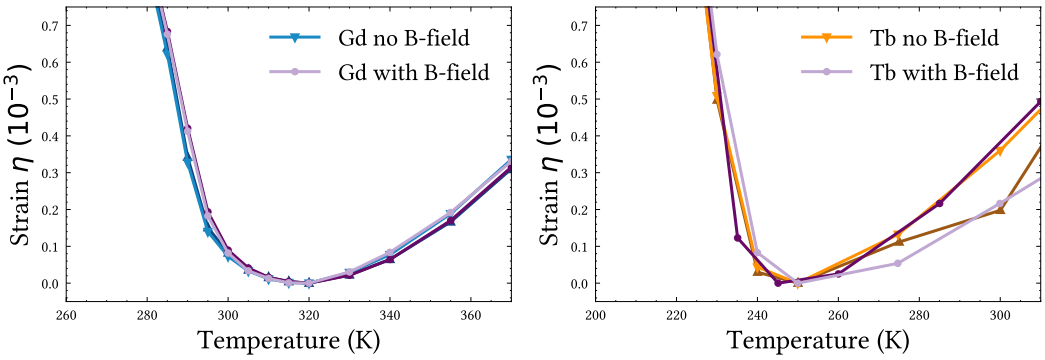

(a) **(b)**

Figure 6.1: (a) A possible forced magnetostrictive effect below the magnetic ordering temperature of the 40 nm thin-film Gd has been found when an external 140 mT magnetic field is applied. (b) The quasi-static strain data for the Tb layer has a signal-to-noise ratio that is too low to make a reliable statement about the effect of forced magnetostriction.

The forced magnetostrictive effect could not be confirmed yet, because the temperature-resolved strain measurements of the Gd and Tb layer with and without an applied external magnetic field provide very similar results. In figure 6.1 (a), the strain decreases at a few Kelvin higher temperatures, when an in-plane magnetic field is applied, but above the magnetic ordering temperature, no clear trend can be identified. In order to achieve a more significant effect, a stronger external in-plane magnetic field would be needed to verify the effect of forced magnetostriction.

Another open question is why the magnetic strain behaves differently in Gd, Tb and Dy. The magnetic strain was already quantified by Kittel [57], who presented equation (6.1):

$$\eta_{\text{mag}} = \frac{r}{Y}\frac{\partial J}{\partial r}M^2\cos(\phi) \sim \frac{\partial J}{\partial r}. \tag{6.1}$$

Here, r is the inter atomic distance which is not necessarily the atomic distance out-of-plane, Y is Young's modulus and M is the magnetisation. The magnetic strain η_{mag} is proportional to the change of the exchange coefficient $J(r)$, which can be described by the RKKY interaction (see section 2.1). The exchange coefficient and its derivative in respect to r for Gd, Tb and Dy is illustrated in figure 6.2.

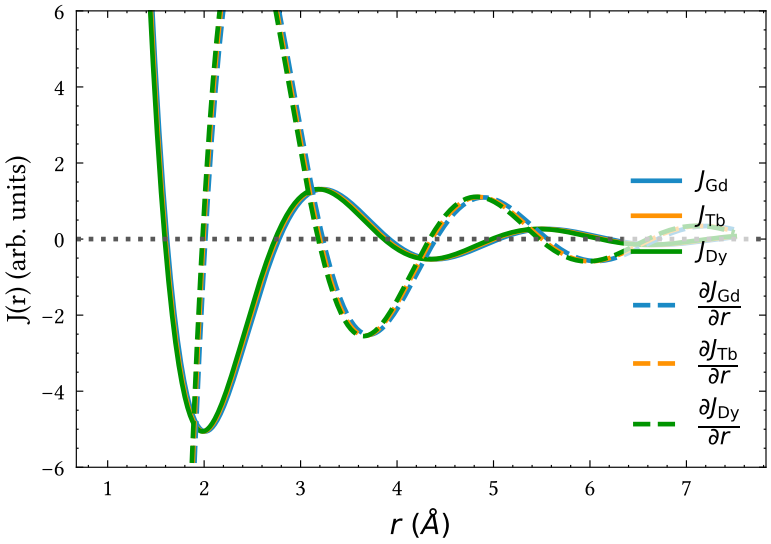

Figure 6.2: The exchange coefficient $J(r)$ has been calculated, under the assumption of a spherical Fermi surface with the radius k_F.

The calculated exchange coefficients for Gd, Tb, and Dy are very similar, and so are their derivatives. This is based on the assumption that the Fermi surfaces are perfect spheres, which is not the case in reality. The Fermi radius k_F was calculated via:

$$k_F = \left(3\pi^2 n\right)^{\frac{1}{3}}. \tag{6.2}$$

n is the electron number density, which is similar for all three rare earths. In a first approximation, the differences in $\partial J/\partial r$ do not appear to account for the variation

in magnetic strain. However, a more accurate representation of the actual Fermi surfaces could alter this conclusion. According to equation (6.1), the magnetic strain η_{mag} is also proportional to M^2, which is different for Gd, Tb and Dy. Equation (6.1) also does not account for nearest neighbour interactions, which at least for Dy have to be relevant, as it is a helical antiferromagnet. To address these uncertainties, a valuable next step would be to model the ultrafast transient strain below the magnetic ordering temperatures of Gd, Tb, and Dy. Simulations of this kind have already been conducted for Dy by von Reppert *et al.* [24]. The modelling for Gd and Tb proved to be a challenge, as the magnetic Grüneisen parameters for these materials are not constant. A possible solution is to approximate the magnetic Grüneisen parameter with two linear functions.

Bibliography

1. Gross, R. & Marx, A. **Festkörperphysik**. ISBN: 978-3-486-71486-9. https://www.degruyter.com/document/doi/10.1524/9783486714869/html (Oldenbourg Wissenschaftsverlag, 2012) (see pages 1, 7, 10, 13, 14, 19, 26, 44, 68).
2. Wood, R. **Future hard disk drive systems**. *Journal of Magnetism and Magnetic Materials. Current Perspectives: Perpendicular Recording* **321,** 555–561. ISSN: 0304-8853. https://www.sciencedirect.com/science/article/pii/S0304885308007877. 2009 (see page 1).
3. Pudell, J., von Reppert, A., Schick, D., Zamponi, F., Rössle, M., Herzog, M., Zabel, H. & Bargheer, M. **Ultrafast negative thermal expansion driven by spin disorder**. *Physical Review B* **99,** 094304. https://link.aps.org/doi/10.1103/PhysRevB.99.094304. 2019 (see pages 1, 5, 39, 49, 51).
4. Von Reppert, A., Mattern, M., Pudell, J.-E., Zeuschner, S. P., Dumesnil, K. & Bargheer, M. **Unconventional picosecond strain pulses resulting from the saturation of magnetic stress within a photoexcited rare earth layer**. *Structural Dynamics* **7,** 024303. ISSN: 2329-7778. https://doi.org/10.1063/1.5145315. 2020 (see pages 1, 5, 17, 39, 42, 51).
5. Mattern, M., von Reppert, A., Zeuschner, S. P., Herzog, M., Pudell, J.-E. & Bargheer, M. **Concepts and use cases for picosecond ultrasonics with x-rays**. *Photoacoustics* **31,** 100503. ISSN: 2213-5979. https://www.sciencedirect.com/science/article/pii/S2213597923000563. 2023 (see pages 1, 5, 11, 17).
6. Mattern, M., Pudell, J.-E., Dumesnil, K., von Reppert, A. & Bargheer, M. **Towards shaping picosecond strain pulses via magnetostrictive transducers**. *Photoacoustics* **30,** 100463. ISSN: 2213-5979. https://www.sciencedirect.com/science/article/pii/S2213597923000162. 2023 (see pages 1, 5).
7. Korff Schmising, C. v., Harpoeth, A., Zhavoronkov, N., Ansari, Z., Aku-Leh, C., Woerner, M., Elsaesser, T., Bargheer, M., Schmidbauer, M., Vrejoiu, I., Hesse, D. & Alexe, M. **Ultrafast magnetostriction and phonon-mediated stress in a photoexcited ferromagnet**. *Physical Review B* **78,** 060404. https://link.aps.org/doi/10.1103/PhysRevB.78.060404. 2008 (see page 1).

8. Reid, A. H., Shen, X., Maldonado, P., Chase, T., Jal, E., Granitzka, P. W., Carva, K., Li, R. K., Li, J., Wu, L., Vecchione, T., Liu, T., Chen, Z., Higley, D. J., Hartmann, N., Coffee, R., Wu, J., Dakovski, G. L., Schlotter, W. F., Ohldag, H., Takahashi, Y. K., Mehta, V., Hellwig, O., Fry, A., Zhu, Y., Cao, J., Fullerton, E. E., Stöhr, J., Oppeneer, P. M., Wang, X. J. & Dürr, H. A. **Beyond a phenomenological description of magnetostriction**. *Nature Communications* **9,** 388. ISSN: 2041-1723. https://www.nature.com/articles/s41467-017-02730-7. 2018 (see page 1).

9. Malinowski, G., Dalla Longa, F., Rietjens, J. H. H., Paluskar, P. V., Huijink, R., Swagten, H. J. M. & Koopmans, B. **Control of speed and efficiency of ultrafast demagnetization by direct transfer of spin angular momentum**. *Nature Physics* **4,** 855–858. ISSN: 1745-2481. https://www.nature.com/articles/nphys1092. 2008 (see page 1).

10. Rudolf, D., La-O-Vorakiat, C., Battiato, M., Adam, R., Shaw, J. M., Turgut, E., Maldonado, P., Mathias, S., Grychtol, P., Nembach, H. T., Silva, T. J., Aeschlimann, M., Kapteyn, H. C., Murnane, M. M., Schneider, C. M. & Oppeneer, P. M. **Ultrafast magnetization enhancement in metallic multilayers driven by superdiffusive spin current**. *Nature Communications* **3,** 1037. ISSN: 2041-1723. https://www.nature.com/articles/ncomms2029. 2012 (see page 1).

11. Wietstruk, M., Melnikov, A., Stamm, C., Kachel, T., Pontius, N., Sultan, M., Gahl, C., Weinelt, M., Dürr, H. A. & Bovensiepen, U. **Hot-Electron-Driven Enhancement of Spin-Lattice Coupling in Gd and Tb $4f$ Ferromagnets Observed by Femtosecond X-Ray Magnetic Circular Dichroism**. *Physical Review Letters* **106,** 127401. https://link.aps.org/doi/10.1103/PhysRevLett.106.127401. 2011 (see pages 1, 51, 62, 64, 67).

12. Thielemann-Kühn, N., Schick, D., Pontius, N., Trabant, C., Mitzner, R., Holldack, K., Zabel, H., Föhlisch, A. & Schüßler-Langeheine, C. **Ultrafast and Energy-Efficient Quenching of Spin Order: Antiferromagnetism Beats Ferromagnetism**. *Physical Review Letters* **119,** 197202. https://link.aps.org/doi/10.1103/PhysRevLett.119.197202. 2017 (see page 1).

13. Frietsch, B., Donges, A., Carley, R., Teichmann, M., Bowlan, J., Döbrich, K., Carva, K., Legut, D., Oppeneer, P. M., Nowak, U. *et al.* **The role of ultrafast magnon generation in the magnetization dynamics of rare-earth metals**. *Science advances* **6,** eabb1601. 2020 (see page 1).

14. Zamponi, F., Ansari, Z., v. Korff Schmising, C., Rothhardt, P., Zhavoronkov, N., Woerner, M., Elsaesser, T., Bargheer, M., Trobitzsch-Ryll, T. & Haschke, M. **Femtosecond hard X-ray plasma sources with a kilohertz repetition rate**. *Applied Physics A* **96,** 51–58. ISSN: 1432-0630. https://doi.org/10.1007/s00339-009-5171-9. 2009 (see pages 2, 52).

15. Schick, D., Bojahr, A., Herzog, M., Schmising, C. v. K., Shayduk, R., Leitenberger, W., Gaal, P. & Bargheer, M. **Normalization schemes for ultrafast x-ray diffraction using a table-top laser-driven plasma source**. *Review of Scientific Instruments* **83,** 025104. ISSN: 0034-6748. https://doi.org/10.1063/1.3681254. 2012 (see pages 2, 52).

16. Hunklinger, S. **Festkörperphysik**. ISBN: 978-3-486-59641-0. https://www.degruyter.com/document/doi/10.1524/9783486596410/html (Oldenbourg Wissenschaftsverlag, 2009) (see pages 7, 10, 13, 19, 20, 23, 27).

17. Skomski, R. **Simple Models of Magnetism**. 366 pp. ISBN: 978-0-19-857075-2 (OUP Oxford, 2008) (see page 7).

18. Ott, H. **Magnetic Structures and Phase Transitions in Thin and Ultrathin Films of Heavy Lanthanide Metals Investigated by Resonant Magnetic X-Ray Scattering** (2004). https://refubium.fu-berlin.de/handle/fub188/8711 (see pages 9, 10).

19. Engdahl, G. **Physics of Giant Magnetostriction**, 1–125. ISBN: 978-0-12-238640-4. https://www.sciencedirect.com/science/article/pii/B9780122386404500176 (Academic Press, San Diego, 2000) (see pages 8, 10).

20. Mattern, M., Pudell, J.-E., Laskin, G., von Reppert, A. & Bargheer, M. **Analysis of the temperature- and fluence-dependent magnetic stress in laser-excited SrRuO3**. *Structural Dynamics* **8,** 024302. ISSN: 2329-7778. https://doi.org/10.1063/4.0000072. 2021 (see page 15).

21. Von Reppert, A. **Magnetic strain contributions in laser-excited metals studied by time-resolved X-ray diffraction**. PhD thesis (Universität Potsdam, 2021). https://publishup.uni-potsdam.de/frontdoor/index/index/docId/53558 (see page 29).

22. Zeuschner, S. P. **Magnetoacoustics observed with Ultrafast X-ray Diffraction**. PhD thesis (Universität Potsdam, 2022). https://www.uni-potsdam.de/en/udkm/publications/dissertations-theses (see pages 30, 32, 52).

23. Zeuschner, S. P., Mattern, M., Pudell, J.-E., von Reppert, A., Rössle, M., Leitenberger, W., Schwarzkopf, J., Boschker, J. E., Herzog, M. & Bargheer, M. **Reciprocal space slicing: A time-efficient approach to femtosecond x-ray diffraction**. *Structural Dynamics* **8,** 014302. ISSN: 2329-7778. https://doi.org/10.1063/4.0000040. 2021 (see pages 30, 31, 33, 34).

24. Von Reppert, A., Pudell, J., Koc, A., Reinhardt, M., Leitenberger, W., Dumesnil, K., Zamponi, F. & Bargheer, M. **Persistent nonequilibrium dynamics of the thermal energies in the spin and phonon systems of an antiferromagnet**. *Structural Dynamics* **3,** 054302. ISSN: 2329-7778. https://doi.org/10.1063/1.4961253. 2016 (see pages 39, 64, 72).

25. Rössle, M., Leitenberger, W., Reinhardt, M., Koç, A., Pudell, J., Kwamen, C. & Bargheer, M. **The time-resolved hard X-ray diffraction endstation KMC-3 XPP at BESSY II**. *Journal of Synchrotron Radiation* **28,** 948–960. ISSN: 1600-5775. https://journals.iucr.org/s/issues/2021/03/00/yi5103/. 2021 (see pages 39, 40).

26. Darnell, F. J. **Temperature Dependence of Lattice Parameters for Gd, Dy, and Ho**. *Physical Review* **130,** 1825–1828. https://link.aps.org/doi/10.1103/PhysRev.130.1825. 1963 (see pages 41, 42).

27. Darnell, F. J. **Lattice Parameters of Terbium and Erbium at Low Temperatures**. *Physical Review* **132,** 1098–1100. https://link.aps.org/doi/10.1103/PhysRev.132.1098. 1963 (see pages 41, 42).

28. Koç, A., Reinhardt, M., Reppert, A. v., Rössle, M., Leitenberger, W., Gleich, M., Weinelt, M., Zamponi, F. & Bargheer, M. **Grueneisen-approach for the experimental determination of transient spin and phonon energies from ultrafast x-ray diffraction data: gadolinium**. *Journal of Physics: Condensed Matter* **29,** 264001. ISSN: 0953-8984. https://dx.doi.org/10.1088/1361-648X/aa7187. 2017 (see pages 42, 46, 47, 51, 64, 69).

29. Griffel, M., Skochdopole, R. E. & Spedding, F. H. **The Heat Capacity of Gadolinium from 15 to 355°K**. *Physical Review* **93,** 657–661. https://link.aps.org/doi/10.1103/PhysRev.93.657. 1954 (see page 43).

30. Jennings, L. D., Stanton, R. M. & Spedding, F. H. **Heat Capacity of Terbium from 15 to 350°K**. *The Journal of Chemical Physics* **27,** 909–913. ISSN: 0021-9606. https://doi.org/10.1063/1.1743878. 1957 (see page 43).

31. Griffel, M., Skochdopole, R. E. & Spedding, F. H. **Heat Capacity of Dysprosium from 15 to 300°K**. *The Journal of Chemical Physics* **25,** 75–79. ISSN: 0021-9606. https://doi.org/10.1063/1.1742851. 1956 (see page 43).

32. Jennings, L. D., Miller, R. E. & Spedding, F. H. **Lattice Heat Capacity of the Rare Earths. Heat Capacities of Yttrium and Lutetium from 15-350°K**. *Journal of Chemical Physics* **33,** 1849–1852. ISSN: 0021-9606. https://ui.adsabs.harvard.edu/abs/1960JChPh..33.1849J. 1960 (see page 43).

33. Dan'kov, S. Y., Tishin, A. M., Pecharsky, V. K. & Gschneidner, K. A. **Magnetic phase transitions and the magnetothermal properties of gadolinium**. *Physical Review B* **57,** 3478–3490. https://link.aps.org/doi/10.1103/PhysRevB.57.3478. 1998 (see pages 44, 50).

34. Jayasuriya, K. D., Stewart, A. M., Campbell, S. J. & Gopal, E. S. R. **The critical specific heat of terbium**. *Journal of Physics F: Metal Physics* **14,** 1725. ISSN: 0305-4608. https://dx.doi.org/10.1088/0305-4608/14/7/020. 1984 (see page 44).

35. Pecharsky, V. K., Gschneidner, J. & Fort, D. **Superheating and other unusual observations regarding the first order phase transition in Dy**. *Scripta Materialia* **35.** https://www.osti.gov/biblio/382485. 1996 (see page 44).

36. Mattern, M. **Grüneisen model of ultrafast stress in magnetic Materials: Evidence from ultrafast X-ray diffraction experiments**. Master's Thesis (Universität Potsdam, 2020). https://www.uni-potsdam.de/en/udkm/publications/dissertations-theses (see page 49).

37. Haynes, W. M. **CRC Handbook of Chemistry and Physics** 97th ed. 2670 pp. ISBN: 978-1-315-38047-6 (CRC Press, Boca Raton, 2016) (see pages 50, 68).

38. Fisher, E., Manghnani, M. & Kikuta, R. **Hydrostatic pressure derivatives of the single crystal elastic moduli of Gd, Dy and Er**. *Journal of Physics and Chemistry of Solids* **34,** 687–703. 1973 (see pages 50, 68).

39. Salama, K., Brotzen, F. & Donoho, P. **Elastic constants of terbium between 78 and 300 K**. *Journal of Applied Physics* **43,** 3254–3258. ISSN: 0021-8979. https://doi.org/10.1063/1.1661702. 1972 (see pages 50, 68).

40. Wazzan, A. R., Vitt, R. S. & Robinson, L. B. **Pressure Dependence of the Magnetic Transition Temperatures in Terbium from Resistance Measurements**. *Physical Review* **159,** 400–408. https://link.aps.org/doi/10.1103/PhysRev.159.400. 1967 (see page 50).

41. Schick, D. **udkm1Dsim – a Python toolbox for simulating 1D ultrafast dynamics in condensed matter**. *Computer Physics Communications* **266,** 108031. ISSN: 0010-4655. https://www.sciencedirect.com/science/article/pii/S0010465521001430. 2021 (see pages 51, 55, 69).

42. Lawrence Berkeley National Laboratory. **X-ray Data Booklet** 3rd. https://xdb.lbl.gov/ (University of California, Berkeley, 2009) (see page 51).

43. Bargheer, M., Zhavoronkov, N., Bruch, R., Legall, H., Stiel, H., Woerner, M. & Elsaesser, T. **Comparison of focusing optics for femtosecond X-ray diffraction**. *Applied Physics B* **80,** 715–719. ISSN: 1432-0649. https://doi.org/10.1007/s00340-005-1792-7. 2005 (see page 51).

44. Graff, K. F. **Wave Motion in Elastic Solids**. 690 pp. ISBN: 978-0-486-13957-9 (Courier Corporation, 2012) (see page 58).

45. ROYER, D. & Dieulesaint, E. **Elastic Waves in Solids I: Free and Guided Propagation**. 394 pp. ISBN: 978-3-540-65932-7 (Springer Science & Business Media, 1999) (see page 58).

46. Koç, A. **Ultrafast x-ray studies on the non-equilibrium of the magnetic and phononic system in heavy rare-earths**. PhD thesis (Universität Potsdam, 2018). https://publishup.uni-potsdam.de/frontdoor/index/index/docId/42328 (see page 60).

47. Ho, C. Y., Powell, R. W. & Liley, P. E. **Thermal Conductivity of the Elements**. *Journal of Physical and Chemical Reference Data* **1,** 279–421. ISSN: 0047-2689. https://doi.org/10.1063/1.3253100. 1972 (see page 68).

48. Adachi, S. **The Handbook on Optical Constants of Metals: In Tables and Figures**. 684 pp. ISBN: 978-981-4405-94-2 (World Scientific, 2012) (see page 68).

49. Lewis, J., Schwarzenbach, D. & Flack, H. **Electric field gradients and charge density in corundum, α-Al2O3**. *Acta Crystallographica Section A: Crystal Physics, Diffraction, Theoretical and General Crystallography* **38,** 733–739. 1982 (see page 68).

50. Roberge, R. **Lattice parameter of niobium between 4.2 and 300 K**. *Journal of the Less Common Metals* **40,** 161–164. ISSN: 0022-5088. https://www.sciencedirect.com/science/article/pii/0022508875901939. 1975 (see page 68).

51. Lucht, M., Lerche, M., Wille, H.-C., Shvyd'Ko, Y. V., Rüter, H., Gerdau, E. & Becker, P. **Precise measurement of the lattice parameters of α-Al2O3 in the temperature range 4.5–250 K using the Mössbauer wavelength standard**. *Journal of applied crystallography* **36,** 1075–1081. 2003 (see page 68).

52. Ginnings, D. C. & Furukawa, G. T. **Heat Capacity Standards for the Range 14 to 1200°K.** *Journal of the American Chemical Society* **75,** 522–527. ISSN: 0002-7863, 1520-5126. https://pubs.acs.org/doi/abs/10.1021/ja01099a004. 1953 (see page 68).

53. Dobrovinskaya, E. R., Lytvynov, L. A. & Pishchik, V. **Sapphire: Material, Manufacturing, Applications**. 493 pp. ISBN: 978-0-387-85695-7 (Springer Science & Business Media, 2009) (see page 68).

54. Smith, J. F. & Gjevre, J. A. **Elastic Constants of Yttrium Single Crystals in the Temperature Range 4.2–400°K**. *Journal of Applied Physics* **31,** 645–647. ISSN: 0021-8979. https://doi.org/10.1063/1.1735657. 1960 (see page 68).

55. Carroll, K. J. **Elastic Constants of Niobium from 4.2° to 300°K**. *Journal of Applied Physics* **36,** 3689–3690. ISSN: 0021-8979. https://doi.org/10.1063/1.1703072. 1965 (see page 68).

56. Hovis, D. B., Reddy, A. & Heuer, A. H. **X-ray elastic constants for α-Al2O3**. *Applied Physics Letters* **88,** 131910. ISSN: 0003-6951. https://doi.org/10.1063/1.2189071. 2006 (see page 68).

57. Kittel, C. **Model of Exchange-Inversion Magnetization**. *Physical Review* **120,** 335–342. https://link.aps.org/doi/10.1103/PhysRev.120.335. 1960 (see page 71).

Declaration of Authorship

I hereby declare that this thesis is my own unaided work. All direct or indirect sources used are acknowledged as references.

Berlin, 11th November 2024

Florian Baltrusch